

Metal–Organic Framework Based Hydrogen-Bonding Nanotrap for Efficient Acetylene Storage and Separation

Yingxiang Ye,[●] Shikai Xian,[●] Hui Cui, Kui Tan, Lingshan Gong, Bin Liang, Tony Pham, Haardik Pandey, Rajamani Krishna, Pui Ching Lan, Katherine A. Forrest, Brian Space, Timo Thonhauser, Jing Li,^{*} and Shengqian Ma^{*}



Cite This: *J. Am. Chem. Soc.* 2022, 144, 1681–1689



Read Online

ACCESS |



Metrics & More

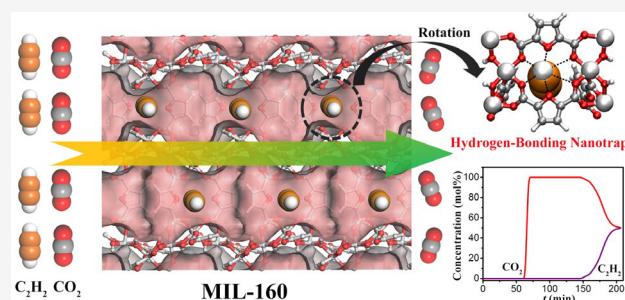


Article Recommendations



Supporting Information

ABSTRACT: The removal of carbon dioxide (CO₂) from acetylene (C₂H₂) is a critical industrial process for manufacturing high-purity C₂H₂. However, it remains challenging to address the tradeoff between adsorption capacity and selectivity, on account of their similar physical properties and molecular sizes. To overcome this difficulty, here we report a novel strategy involving the regulation of a hydrogen-bonding nanotrap on the pore surface to promote the separation of C₂H₂/CO₂ mixtures in three isostructural metal–organic frameworks (MOFs, named MIL-160, CAU-10H, and CAU-23, respectively). Among them, MIL-160, which has abundant hydrogen-bonding acceptors as nanotraps, can selectively capture acetylene molecules and demonstrates an ultrahigh C₂H₂ storage capacity (191 cm³ g⁻¹, or 213 cm³ cm⁻³) but much less CO₂ uptake (90 cm³ g⁻¹) under ambient conditions. The C₂H₂ adsorption amount of MIL-160 is remarkably higher than those for the other two isostructural MOFs (86 and 119 cm³ g⁻¹ for CAU-10H and CAU-23, respectively) under the same conditions. More importantly, both simulation and experimental breakthrough results show that MIL-160 sets a new benchmark for equimolar C₂H₂/CO₂ separation in terms of the separation potential ($\Delta q_{\text{break}} = 5.02$ mol/kg) and C₂H₂ productivity (6.8 mol/kg). In addition, *in situ* FT-IR experiments and computational modeling further reveal that the unique host–guest multiple hydrogen-bonding interaction between the nanotrap and C₂H₂ is the key factor for achieving the extraordinary acetylene storage capacity and superior C₂H₂/CO₂ selectivity. This work provides a novel and powerful approach to address the tradeoff of this extremely challenging gas separation.



INTRODUCTION

Gas separation and purification are crucial processes in the chemical industry to manufacture polymers, fuel, and plastics.^{1–4} Acetylene (C₂H₂) is not only an important gaseous fuel but also a fundamental building block for modern commodity chemicals.⁵ However, impurity components (e.g., CO₂) are inevitably produced during the production of acetylene.⁶ Since these two gas molecules have very similar molecular sizes/shapes (C₂H₂, 3.34 × 3.32 × 5.70 Å³; CO₂, 3.33 × 3.18 × 5.36 Å³) and physical properties (boiling points: C₂H₂, 189.3 K; CO₂, 194.7 K),⁷ the separation of a C₂H₂/CO₂ mixture is one of the most challenging separation tasks.^{8–10} In recent years, a gas separation approach based on the physical adsorption of porous adsorbents has attracted extensive attention due to its low cost and energy-saving prospects,^{11–15} in comparison to the traditionally energy intensive cryogenic distillation technology.¹⁶

The emerging metal–organic frameworks (MOFs)^{17–23} feature high modularity, large surface areas, and abundant functionality, in comparison with traditional solid adsorbents (e.g., zeolite and activated carbon).^{24,25} They can be readily constructed by combining metal ions/clusters with organic

linkers through coordination linkages^{26,27} and have been well demonstrated to be promising in addressing many important gas separations (e.g., flue gas, olefin/paraffin).^{28–35} It is a daunting challenge for a porous adsorbent in gas separation and purification to have both a high storage capacity and a high selectivity, the so-called tradeoff. For instance, MOFs with a high density of open metal sites (OMS; e.g., MOF-74 and HKUST-1) can improve the storage capacity of C₂H₂; however, it has also been shown that a high affinity for CO₂ can result in lower separation selectivity.^{36–39} On the other hand, several ultramicroporous MOFs exhibit a high separation selectivity of C₂H₂/CO₂ yet have a limited acetylene uptake capacity.^{40–43} Therefore, there is an added value to develop an effective approach to address this tradeoff and achieve efficient separation of C₂H₂/CO₂ mixtures.

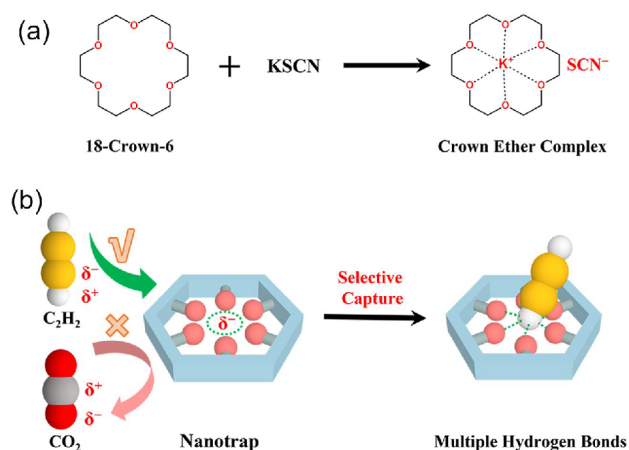
Received: October 7, 2021

Published: December 29, 2021



Due to their nearly identical kinetic diameters (ca. 3.3 Å), effective separation of a C₂H₂/CO₂ mixture cannot be achieved simply through fine-tuning the pore size, unlike the case for other gaseous mixtures (e.g., CO₂/CH₄, alkyne/alkene).^{44,45} Notably, there is a significant difference in the quadrupole moments and electrostatic potentials of carbon dioxide and acetylene (-13.4×10^{-40} and $+20.5 \times 10^{-40}$ C m² for CO₂ and C₂H₂; Figure S1).^{46,47} Thus, it is essential to fabricate specific functional sites within the porous MOFs that can preferentially bind with C₂H₂ over CO₂. Inspired by the concept of specific recognition of crown ether complexes and macrocyclic molecules (Scheme 1a),^{48–50} we hypothesize that

Scheme 1. (a) Crown Ether Complex According to Pedersen⁴⁸ and (b) Selective Capture by a Hydrogen-Bonding Nanotrap of a Target Molecule through Host–Guest Multiple Hydrogen-Bonding Interactions



if the hydrogen-bonding nanotrap⁵¹ (as acceptor) is immobilized on the pore surface of porous MOFs, it will not only provide strong hydrogen-bonding interactions to capture acetylene molecules (as donors) but also would not sacrifice the intrinsic pore volume (Scheme 1b).

In this regard, MIL-160, first reported by Serre and co-workers,⁵² containing high-density hydrogen-bonding nanotraps within the pore surfaces, could be a promising candidate to achieve the aforementioned mission. To further demonstrate our strategy, here we synthesized three isostructural aluminum-based MOFs (named MIL-160, CAU-10H, and CAU-23, respectively)^{52–54} on the basis of the isoreticular features of MOF chemistry and explored their binding abilities for C₂H₂ and C₂H₂/CO₂ separation selectivity for comparison. As expected, MIL-160 with the highest density hydrogen-bonding nanotraps has an excellent C₂H₂ storage capacity (191 cm³ g⁻¹, or 213 cm³ cm⁻³) but a much lower uptake of CO₂ (90 cm³ g⁻¹) at 298 K and 100 kPa. Notably, the separation performance (storage capacity and selectivity) for C₂H₂/CO₂ mixtures in MIL-160 is significantly higher than that of CAU-10H and CAU-23. Meanwhile, the simulation and experimental breakthroughs have fully demonstrated MIL-160 to be the best porous adsorbent reported thus far for equimolar C₂H₂/CO₂ separation with regard to the separation potential ($\Delta q_{\text{break}} = 5.02$ mol/kg) and C₂H₂ productivity (6.8 mol/kg). Moreover, computational modeling studies and *in situ* FT-IR tests both reveal that the ultrahigh acetylene storage capacity and superior C₂H₂/CO₂ selectivity of MIL-160 can be mainly attributed to the unique host–guest multiple interactions

between the hydrogen-bonding nanotrap and C₂H₂ molecule. This research provides a novel perspective to address the tradeoff for this challenging gas separation.

RESULTS AND DISCUSSION

In these three isostructural MOFs MIL-160, CAU-10H, and CAU-23, each Al(III) atom is coordinated by six O atoms from two hydroxyl and four carboxylate groups, respectively, with a typical AlO₆ octahedral geometry. Notably, in MIL-160 and CAU-10H, the two hydroxyl groups lie in *cis* positions, bridge the adjacent Al centers through a vertex-sharing mode, and form a 1D helical chain secondary building unit (SBU) along the *c* axis (Figure 1, top left). In contrast, another type of 1D

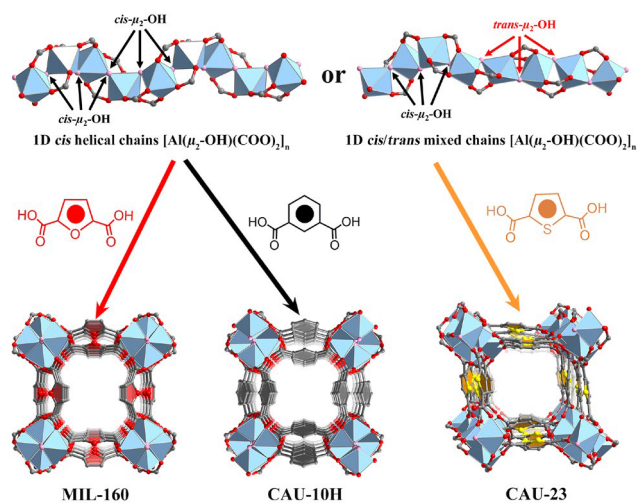


Figure 1. 1D chains $[\text{Al}(\mu_2\text{-OH})(\text{COO})_2]_n$ and V-shaped ligands (H₂FDC, m-H₂BDC, and H₂TDC) assemble into three isostructural 3D frameworks of MIL-160, CAU-10H, and CAU-23, respectively. Hydrogen atoms are omitted for clarity. Color code, Al: pale blue; O, red and rose; C, 50% gray.

chain SBU in CAU-23 is formed by four consecutive alternating units of *trans* and *cis* corner-sharing AlO₆ octahedra; this constructs a novel straight and helical mixed chain (Figure 1, top right). The above two types of 1D chains are quite different from the linear 1D chain with *trans*-connected mode in MIL-53 series of MOFs.⁵⁵ These 1D chains are further linked to four adjacent chains by the V-shaped ligands (FDC, m-BDC, and TDC) and extended into a three-dimensional (3D) open framework of MIL-160, CAU-10H, and CAU-23, respectively. After removal of the guest molecules, these three isostructural MOFs exhibit one-dimensional (1D) square channels, with pore aperture sizes of 4.6 × 9.8, 3.6 × 9.2, and 6.3 × 7.6 Å², respectively (Figures S3–S5). Furthermore, some basic characteristics (e.g., FT-IR, TGA, and PXRD) of these three MOFs are provided in Figures S6–S14 (see the Supporting Information for details).

The permanent porous behaviors of these three MOFs were first investigated at 77 K with N₂ adsorption experiments. All of them exhibit a fully reversible type I adsorption behavior, with Brunauer–Emmett–Teller (BET) surface areas of 1138, 680, and 1320 m² g⁻¹ for MIL-160, CAU-10H, and CAU-23, respectively (Figures S15–S17), which are consistent with the previously reported values.^{52–54} In addition, the pore-size distributions (PSD) of these three MOFs were analyzed by employing the 77 K N₂ isotherms according to the Horvath–

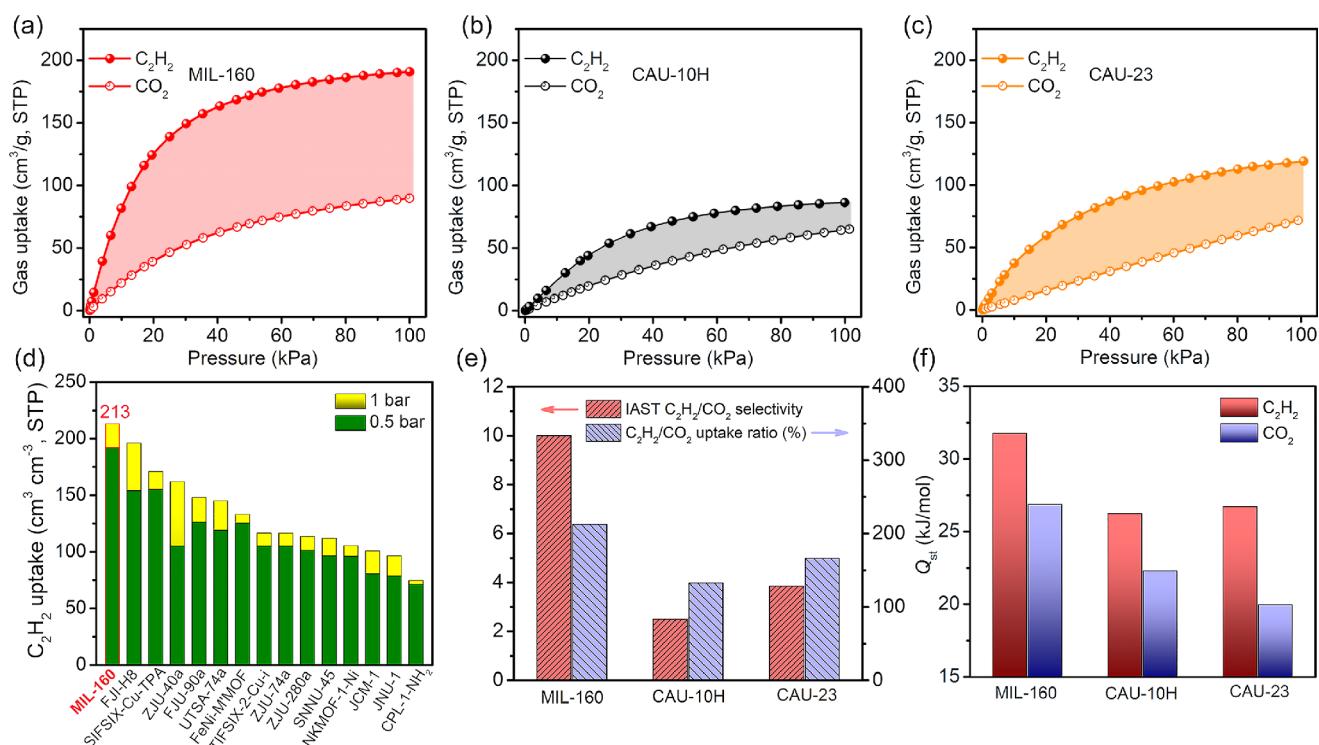


Figure 2. (a–c) Single-component C₂H₂ and CO₂ adsorption isotherms of MIL-160, CAU-10H, and CAU-23, respectively, at 298 K under 100 kPa. (d) C₂H₂ volumetric uptake of MIL-160 in comparison to other best-performing MOF materials for C₂H₂/CO₂ separation at room temperature. (e) Comparison of C₂H₂/CO₂ selectivity and uptake ratio among these three MOFs at 298 K and 100 kPa. (f) Comparison of the heat of adsorption (Q_{st}) of C₂H₂ and CO₂ at near-zero coverage for MIL-160, CAU-10H, and CAU-23.

Kawazoe cylinder model. All of them display narrow pore size distributions with main peaks at 7.0, 6.0, and 6.8 Å, respectively (Figure S18), consistent with the pore size determined by the crystal structure.

The permanent porosity and suitable pore size of these three MOFs provide us the initial motivation to explore their adsorption behaviors toward C₂H₂ and CO₂. Therefore, the adsorption isotherms of C₂H₂ and CO₂ were collected at 273 and 298 K under 100 kPa pressure. As shown in Figure 2a–c, the C₂H₂ uptake values at 298 K and 100 kPa are 191, 86, and 119 cm³ g⁻¹ for MIL-160, CAU-10H, and CAU-23, respectively. Notably, the gravimetric C₂H₂ uptake value (191 cm³ g⁻¹) of MIL-160 is remarkably higher than those of the other two isostructural MOFs and is also superior to those of most of the top-performing materials for C₂H₂/CO₂ separation, such as SIFSIX-Cu-TPA (185 cm³ g⁻¹),⁵⁶ FJU-90a (180 cm³ g⁻¹),⁵⁷ UTSA-74a (108 cm³ g⁻¹),⁵⁸ FeNi-M'MOF (96 cm³ g⁻¹),⁵⁹ Cu@FAU (79.5 cm³ g⁻¹),⁶⁰ and Cu^I@UiO-66-(COOH)₂ (52 cm³ g⁻¹)⁴² and is only lower than that of the benchmark material FJI-H8 (224 cm³ g⁻¹),⁶¹ which has high-density open Cu sites under similar conditions (Table S6). In the actual separation process, the role of the volumetric storage capacity is even more important than the corresponding gravimetric capacity because it can make full use of the fixed-bed space and minimize the cost of energy regeneration. Under ambient conditions, MIL-160 exhibits the second highest volumetric C₂H₂ adsorption capacity among the reported porous materials with a value of 213 cm³ cm⁻³. This value is only slightly lower than the record of 230 cm³ cm⁻³ for CoMOF-74 with high-density OMS⁶² and is significantly higher than those of other best-performing C₂H₂/CO₂ separation materials (e.g., 196 cm³ cm⁻³ for FJI-H8,⁶¹ 147

cm³ cm⁻³ for FJU-90a,⁵⁷ and 145 cm³ cm⁻³ for UTSA-74a;⁵⁸ Figure 2d) under similar conditions. For equimolar C₂H₂/CO₂ separation, the uptake value of C₂H₂ at a partial pressure of 0.5 bar is another key indicator that needs to be considered. In this regard, the C₂H₂ volumetric uptake of MIL-160 reaches up to 192 cm³ cm⁻³ (7.7 mmol g⁻¹) at 298 K and 0.5 bar and is also superior to most of the best-performing materials for this separation (Figure 2d).

In addition, the density of the adsorbed acetylene in the channels can be determined as 518, 341, and 262 g/L for MIL-160, CAU-10H, and CAU-23 at 298 K and 100 kPa, respectively, on the basis of their C₂H₂ adsorption capacities and corresponding pore volumes (Table S6). The packing density of C₂H₂ in MIL-160 is notably higher than those of the other two isostructural MOFs and is also about 440 times the density of gaseous C₂H₂ (1.1772 g/L, at 273 K and 101.3 kPa) and is close to the density of solid C₂H₂ at 189 K (729 g/L),⁶³ indicating that the acetylene molecules can be efficiently packed in the channels of MIL-160. On the other hand, MIL-160 shows the second highest safe acetylene storage density (0.247 g cm⁻³, slightly lower than the record of 0.267 g cm⁻³ for CoMOF-74; Table S6) in bulk material at 298 K and 100 kPa, which is about 100 times higher than the safe compression limit (0.2 MPa = 0.0021 g cm⁻³) of C₂H₂ at room temperature.⁸ For the practical application of acetylene storage, a promising adsorbent should have good repeatability and structural stability. Thus, we carried out five consecutive acetylene adsorption–desorption isotherm tests. As expected, there was no loss of C₂H₂ storage capacity in MIL-160 after five cycles at 298 K, indicating that MIL-160 is a promising material in refillable C₂H₂ storage (Figure S39).

In contrast, the CO₂ uptake capacities of MIL-160, CAU-10H, and CAU-23 are only 90, 65, and 72 cm³ g⁻¹, giving C₂H₂/CO₂ uptake ratios of 210%, 130%, and 160% (Figure 2e), respectively, at 100 kPa and 298 K. To further assess the separation performance of MIL-160, CAU-10H, and CAU-23 toward C₂H₂/CO₂ mixtures, the separation selectivity was calculated by using the widely studied ideal adsorbed solution theory (IAST).⁶⁴ As shown in Figure S37b, the IAST selectivity of MIL-160 for equimolar C₂H₂/CO₂ mixtures is up to 10 at 298 K and 100 kPa, which is about 2.6 and 4.0 times higher than the corresponding values in CAU-23 (3.8) and CAU-10H (2.5) and higher than those of some of the benchmark porous MOF materials, such as UTSA-74a (8.2),⁵⁸ FJU-90a (4.3),⁵⁷ MUF-17 (6.0),⁶⁵ SIFSIX-21-Ni (7.8),⁶⁶ and TIFSIX-2-Cu-i (6.5)⁶⁷ under similar conditions. Although some porous materials feature relatively higher C₂H₂/CO₂ selectivity, their adsorption capacity of C₂H₂ is relatively low (usually less than 100 cm³ g⁻¹ under ambient conditions).^{42,43,68} The high uptake ratio and IAST selectivity both suggested the potential of MIL-160 for effective C₂H₂/CO₂ separation.

The affinity between the host framework and the guest molecule can be evaluated by the low-coverage heat of adsorption (Q_{st}). The coverage-dependent Q_{st} values of MIL-160, CAU-10H, and CAU-23 for C₂H₂ and CO₂ were obtained by fitting the single-component gas isotherms collected at 273 and 298 K. As shown in Figure 2f, the near-zero coverage Q_{st} value of C₂H₂ (31.8, 26.2, and 26.7 kJ mol⁻¹ for MIL-160, CAU-10H, and CAU-23, respectively) in these three isostructural MOFs is obviously higher than their corresponding values of CO₂ (26.9, 22.3, and 20.0 kJ mol⁻¹), indicating that these MOFs have a stronger affinity for C₂H₂ over CO₂. Unlike CAU-23, the Q_{st} value of C₂H₂ in MIL-160 and CAU-10H gradually increases with an increase in C₂H₂ loading (Figures S21, S24, and S27). This implies that C₂H₂ molecules may form intermolecular interactions during the adsorption process,^{69–72} which is consistent with the results of high-density C₂H₂ storage in MIL-160 and CAU-10H. Additionally, the Q_{st} value of C₂H₂ in MIL-160 is lower than those of some benchmark porous materials with high density of OMS, such as Cu-ATC (79.1 kJ mol⁻¹),¹⁰ ZJU-74a (45 kJ mol⁻¹),⁷³ Cu¹@UiO-66-(COOH)₂ (74.5 kJ mol⁻¹),⁴² and Cu@FAU (50.0 kJ mol⁻¹).⁶⁰ The moderate Q_{st} value of C₂H₂ indicates that MIL-160 can be regenerated under mild conditions, which give it a great potential for energy-efficient C₂H₂/CO₂ separation.

To accurately evaluate the separation performance of porous materials in a fixed bed, we must consider not only the separation selectivity but also the adsorption capacity. To resolve this dilemma, a combined metric, termed the separation potential (Δq), was defined by Krishna.^{74,75} Subsequently, transient breakthrough simulations were performed for binary 50/50 or 90/10 C₂H₂/CO₂ mixtures in these three MOFs (Figure S40), operating at a total pressure of 100 kPa and 298 K, by employing the previously reported methodology.^{57,74–76} As shown in Figure 3a, the equimolar C₂H₂/CO₂ mixtures can be effectively separated by MIL-160, accompanied by the highest retention time ($\Delta\tau = 304$; Table S2). Moreover, we compared the two types of separation potential (Δq_{break} and Δq_{IAST}) of MIL-160 with those of other top-performing porous materials for C₂H₂/CO₂ separation under ambient conditions (Figure 3b and Table S2).^{57–59,73,77} It is worth noting that MIL-160 has not only the highest Δq_{IAST} (calculated on the basis of the static adsorption

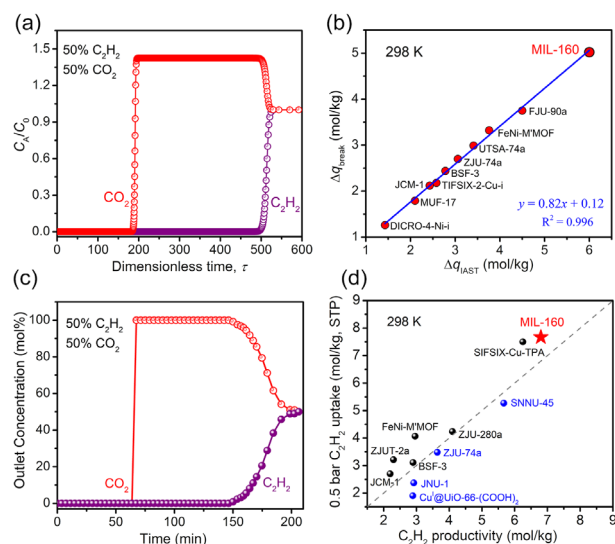


Figure 3. (a) Transient breakthrough curves of equimolar C₂H₂/CO₂ mixtures for MIL-160 at 298 K and 100 kPa. (b) Comparison of the separation potential Δq of MIL-160 with those other benchmark porous materials. Note: the separation potentials Δq_{break} and Δq_{IAST} were calculated on the basis of the transient breakthrough simulations and the static adsorption isotherms for C₂H₂/CO₂ (50/50) mixtures. (c) Experimental breakthrough curves for C₂H₂/CO₂ (50/50) gas mixtures in a laboratory-scale fixed-bed packing with a MIL-160 sample under ambient conditions (298 K, 1 bar). (d) Single-component static C₂H₂ uptake at a partial pressure of 0.5 bar and dynamic C₂H₂ capture amount of equimolar C₂H₂/CO₂ mixtures by MIL-160 in comparison with those of top-performing porous materials at room temperature (black balls, the dotted line, and blue balls indicate that 0.5 bar C₂H₂ uptake is larger than, equal to, and less than dynamic C₂H₂ capture, respectively).

isotherms) value of 6.0 mol/kg for equimolar C₂H₂/CO₂ mixtures but also the highest Δq_{break} (5.02 mol/kg, calculated on the basis of the transient breakthrough simulations) value, indicating that MIL-160 has the best separation ability for this gas mixture. In addition, the separation potentials Δq_{break} and Δq_{IAST} have a good positive linear relationship ($R^2 = 0.996$), with the equation $y = 0.82x + 0.12$. The linear range of this equation is approximately twice that of previously reported results.^{77,78} Therefore, this empirical equation can be used to predict porous materials for challenging C₂H₂/CO₂ separation after their Δq_{IAST} values have been calculated.

The record-high separation potential prompted us to evaluate the separation performance of MIL-160 for challenging C₂H₂/CO₂ mixtures under real conditions. We performed laboratory-scale dynamic breakthrough experiments, with the equimolar C₂H₂/CO₂ mixtures being flowed through a packed column filled with an activated sample (~1.2 g) at a total flow rate of 2 mL min⁻¹ under ambient conditions. As shown in Figure 3c, the C₂H₂/CO₂ mixture can be efficiently separated, in which the CO₂ is eluted first at 64 min and rapidly reaches up to a pure grade without acetylene outflow, and this process continued for ~86 min, a remarkable time to obtain pure CO₂, until the saturated uptake of acetylene and thus breakthrough (at 150 min). According to the breakthrough curve, the dynamic C₂H₂ capture amount (also named productivity) was found to be 6.8 mol/kg for a given cycle, which is highly consistent with the equilibrium adsorption of C₂H₂ under similar conditions (7.7 mol/kg, at 298 K and 0.5 bar). Notably, the dynamic C₂H₂ productivity of

MIL-160 is among the highest values achieved and is much higher than those of most benchmark porous materials (Figure 3d, Table S3), such as FeNi-M'MOF (2.96 mol/kg),⁵⁹ ZJU-74a (3.64 mol/kg),⁷³ and Cu^I@UiO-66-(COOH)₂ (2.89 mol/kg).⁴² Therefore, MIL-160 establishes a new benchmark for the separation of challenging C₂H₂/CO₂ mixtures under actual conditions. Considering the need for recyclability in industrial applications, we carried out a multicycle mixed-gas breakthrough experiment under the same conditions. The results indicate no notable loss in the breakthrough time and C₂H₂ capture capacity of MIL-160 in four consecutive cycles (Figures S41–S43), which proves that it maintains excellent repeatability for C₂H₂/CO₂ separation.

In situ infrared (IR) spectroscopic measurements were conducted to further probe the interaction of C₂H₂ within three MOF structures: namely, MIL-160, CAU-23, and CAU-10H. C₂H₂ is well-known to have an acidic nature and thus tends to form hydrogen bonds within the basic sites, as observed in several MOFs.^{34,79,80} Similar to the well-studied OH stretching vibration,⁸¹ the $\nu_{\text{as}}(\text{C}_2\text{H}_2)$ band undergoes a downward shift with reference to the gas-phase value at 3287 cm⁻¹ when it is subjected to a hydrogen-bonding interaction and the frequency shift is a measure of intermolecular H bonds. Figure 4 presents the stretching band of adsorbed

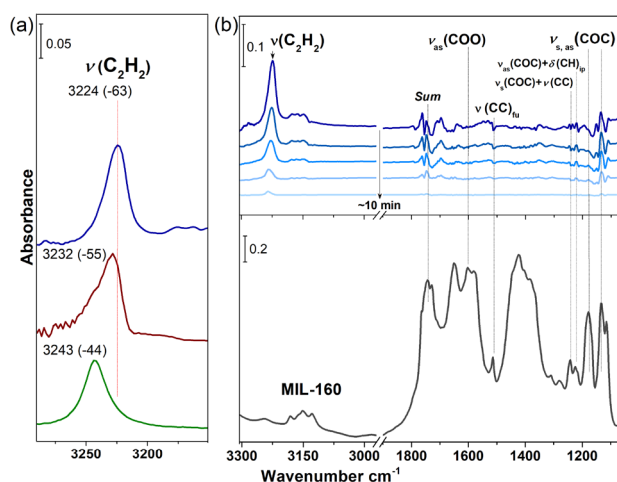


Figure 4. (a) IR spectra showing the stretching band of adsorbed C₂H₂ inside MIL-160 (blue), CAU-23 (brown), and CAU-10 (green) upon loading C₂H₂ gas at ~400 Torr (see full spectra in Figure 4b and Figure S45). The signal of gas-phase C₂H₂ is subtracted. The values in parentheses show the shift of the $\nu_{\text{as}}(\text{C}_2\text{H}_2)$ band with respect to the gas phase at 3287 cm⁻¹. (b) The top five difference spectra showing the unloading of C₂H₂ from MIL-160 upon evacuation of the gas phase for ~10 min; each is referenced to the bottom spectrum of activated MIL-160 under vacuum. Notation and acronyms: ν , stretch; δ , deformation; as, asymmetric; s, symmetric; ip, in plane; sum, summation band; fu, furan ring.

acetylene upon loading C₂H₂ at ~400 Torr into three MOFs and its desorption from MIL-160 after evacuating the gas phase. As shown in Figure 4a, $\nu_{\text{as}}(\text{C}_2\text{H}_2)$ bands occur at 3224, 3232, and 3243 cm⁻¹ in MIL-160, CAU-23, and CAU-10H, respectively. The trend of band position shift indicates that hydrogen-bonding interactions follow the order MIL-160 > CAU-23 > CAU-10H. In addition, different spectra shown in Figure 4b show that vibrational modes associated with the organic linker, including the COC symmetric and asymmetric stretch at 1178 and 1133 cm⁻¹, the coupled COC stretch/CC

stretch/in-plane C–H deformation at 1242–1224 cm⁻¹, the furan ring carbon stretch at 1514 cm⁻¹, the carboxylate asymmetric stretch at 1580–1602 cm⁻¹,⁸² and the out-of-plane C–H summation band at 1743 cm⁻¹,⁸³ are appreciably perturbed upon loading acetylene into MIL-160 (see assignment in Table S4). With desorption of the trapped acetylene from MIL-160, the perturbations of these modes gradually disappeared, as seen in Figure 4b. These observations point to the direct interaction of loaded C₂H₂ molecules with both COO⁻ and the O-containing ring of the FDC linker, as further verified by our modeling studies (Table S4).

To gain insight into the binding sites of C₂H₂ and CO₂ in MIL-160, modeling studies based on simulated annealing calculations and canonical Monte Carlo (CMC) simulations were performed (see the Supporting Information for details). As shown in Figure S46, three and two possible binding sites of C₂H₂ and CO₂ were found in MIL-160, respectively. Here, we focus on discussing and comparing the primary binding site of C₂H₂ and CO₂ in MIL-160, and discussions on other binding sites are provided in the Supporting Information. It was observed that the orientation of the C₂H₂ (I) molecule is roughly perpendicular to the MOF channel (Figure S46a), where it forms multiple H–C≡C–H^{δ+}...O^{δ-} hydrogen-bonding interactions with the nearby carboxylate groups and furan rings, forming a nanotrap on the pore surface, with close interaction distances ranging from 2.51 to 3.57 Å (Figure 5a).

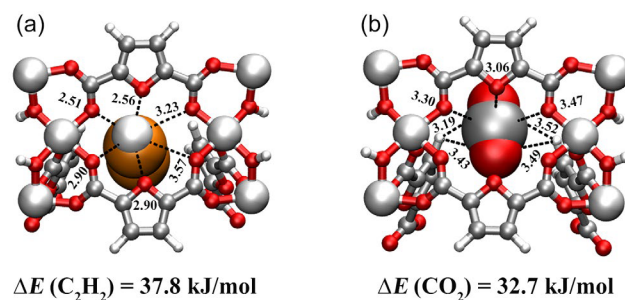


Figure 5. Canonical Monte Carlo (CMC) simulated primary binding sites of (a) C₂H₂ and (b) CO₂ in MIL-160. Distances are given in Å.

In contrast, the CO₂ (I) molecule is oriented parallel to the *c* axis in the channels (Figure S46b),⁸⁴ in which (CO₂)C^{δ+}...O^{δ-} electrostatic interactions with the carboxylate groups and the furan O atom (distances ranging from 3.06 to 3.47 Å) and CH^{δ+}...O^{δ-}(CO₂) interactions with the nearby furan rings (distances ranging from 3.19 to 3.52 Å) were observed (Figure 5b). Overall, C₂H₂ exhibits typically shorter interaction distances with MIL-160 at the primary binding site in comparison to CO₂, which accounts for the stronger affinity of C₂H₂ with the adsorbent. The calculated binding energies (37.8 vs 32.7 kJ mol⁻¹) for single C₂H₂ and CO₂ molecules positioned at their global minimum in MIL-160 from CMC simulations were consistent with the trend in the experimental low-coverage *Q*_{st} values (31.8 vs 26.9 kJ mol⁻¹) from single-component adsorption isotherms (Table S5). In summary, the binding configurations in MIL-160 calculated herein combine key features that cause stronger C₂H₂ binding versus CO₂: multiple H–C≡C–H^{δ+}...O^{δ-} hydrogen-bonding interactions and weak CO₂–sorbsent electrostatic interactions.

The diffusion of C₂H₂ and CO₂ molecules inside MIL-160 was investigated by looking at various transition-state configurations of the molecules traveling through the MOF

channel using the climbing nudged elastic band (cNEB) method.^{85,86} To better understand the interaction taking place during molecular diffusion, induced charge densities were mapped for the initial, transition, and final states, as shown in Figure S48. For the initial configuration (at 0% progress), both C₂H₂ and CO₂ molecules occupy the space near their respective primary binding sites, giving the lowest energy to this configuration. Subsequently, the gas molecules move along the channel, getting to the highest energy configuration with diffusion barriers of 157 meV for C₂H₂ and 161 meV for CO₂, respectively. At the initial state, C₂H₂ and CO₂ show interactions with the MOF linkers, as evidenced by the yellow/blue induced charge densities in Figure S48. However, at the transition configuration CO₂ shows a reduced interaction with the surrounding linkers, as evidenced by the reduction in induced charge density. In contrast, C₂H₂ still exhibits strong interaction with the linker atoms (see Figure S48a for the transition state). This results in a transition configuration that is more stable for C₂H₂ in comparison to CO₂. Therefore, the diffusion energy barrier of C₂H₂ is slightly lower, leading to a faster molecular transport along the MOF channel, indicating that less energy is required for acetylene molecules to leave the strong binding site and diffuse along the MOF channel. The higher binding energy and lower diffusion kinetic barrier well explain the high separation selectivity of C₂H₂/CO₂ in MIL-160.

CONCLUSIONS

To conclude, we have successfully demonstrated that the high-density hydrogen-bonding nanotrap within the pore surface of porous MOFs can achieve highly selective C₂H₂/CO₂ separation. By virtue of the isoreticular principle in MOF chemistry, we can fine-tune the hydrogen-bonding acceptors on the pore surface, as illustrated in three isostructural MOFs. Notably, MIL-160 features the highest density of hydrogen-bonding nanotraps and exhibits a high acetylene storage capacity and superior separation selectivity simultaneously, supplying a new benchmark for C₂H₂/CO₂ separation with an excellent separation potential and high C₂H₂ productivity under ambient conditions. This research provides an outstanding example of a MOF-based hydrogen-bonding nanotrap to address this challenge of gas separation/purification and thus provides a new perspective for rationally designing porous MOF materials in this very active research area.

ASSOCIATED CONTENT

Supporting Information

The Supporting Information is available free of charge at <https://pubs.acs.org/doi/10.1021/jacs.1c10620>.

Material synthesis, characterization details, and additional figures as described in the text (PDF)

AUTHOR INFORMATION

Corresponding Authors

Jing Li – Department of Chemistry and Chemical Biology, Rutgers University, Piscataway, New Jersey 08854, United States; orcid.org/0000-0001-7792-4322; Email: jingli@rutgers.edu

Shengqian Ma – Department of Chemistry, University of North Texas, Denton, Texas 76201, United States; orcid.org/0000-0002-1897-7069; Email: Shengqian.Ma@unt.edu

Authors

Yingxiang Ye – Department of Chemistry, University of North Texas, Denton, Texas 76201, United States; orcid.org/0000-0003-3962-8463

Shikai Xian – Department of Chemistry and Chemical Biology, Rutgers University, Piscataway, New Jersey 08854, United States; Hoffmann Institute of Advanced Materials, Shenzhen Polytechnic, Shenzhen, Guangdong 518055, People's Republic of China

Hui Cui – Department of Chemistry, University of Texas at San Antonio, San Antonio, Texas 78249-0698, United States; orcid.org/0000-0002-9723-4932

Kui Tan – Department of Materials Science & Engineering, University of Texas at Dallas, Richardson, Texas 75080, United States; orcid.org/0000-0002-5167-7295

Lingshan Gong – Department of Chemistry, University of North Texas, Denton, Texas 76201, United States

Bin Liang – Department of Chemistry, University of North Texas, Denton, Texas 76201, United States

Tony Pham – Department of Chemistry, University of South Florida, Tampa, Florida 33620, United States; orcid.org/0000-0001-5654-163X

Haardik Pandey – Department of Physics and Center for Functional Materials, Wake Forest University, Winston-Salem, North Carolina 27109, United States

Rajamani Krishna – Van 't Hoff Institute for Molecular Sciences, University of Amsterdam, 1098 XH Amsterdam, The Netherlands; orcid.org/0000-0002-4784-8530

Pui Ching Lan – Department of Chemistry, University of North Texas, Denton, Texas 76201, United States

Katherine A. Forrest – Department of Chemistry, University of South Florida, Tampa, Florida 33620, United States

Brian Space – Department of Chemistry, North Carolina State University, Raleigh, North Carolina 27695, United States

Timo Thonhauser – Department of Physics and Center for Functional Materials, Wake Forest University, Winston-Salem, North Carolina 27109, United States; orcid.org/0000-0003-4771-7511

Complete contact information is available at: <https://pubs.acs.org/10.1021/jacs.1c10620>

Author Contributions

Y.Y. and S.X. contributed equally to this work.

Notes

The authors declare no competing financial interest.

ACKNOWLEDGMENTS

We acknowledge the Robert A. Welch Foundation (B-0027) and the U.S. National Science Foundation (ECCS- 2029800) for financial support of this work. We also extend our sincere appreciation to the U.S. Department of Energy, Office of Science, Office of Basic Energy Sciences, under Award DE-SC0019902. T.P., K.A.F., and B.S. acknowledge the National Science Foundation (Award No. DMR-1607989), including support from the Major Research Instrumentation Program (Award No. CHE-1531590). Computational resources were made available by a XSEDE Grant (No. TG-DMR090028) and by Research Computing at the University of South Florida. Adam Hogan is also acknowledged for calculating the polarizability for Al³⁺.

REFERENCES

- (1) Li, J. R.; Kuppler, R. J.; Zhou, H. C. Selective gas adsorption and separation in metal-organic frameworks. *Chem. Soc. Rev.* **2009**, *38*, 1477–1504.
- (2) Lin, R.-B.; Xiang, S.; Zhou, W.; Chen, B. Microporous Metal-Organic Framework Materials for Gas Separation. *Chem* **2020**, *6*, 337–363.
- (3) Wu, Y.; Weckhuysen, B. M. Separation and Purification of Hydrocarbons with Porous Materials. *Angew. Chem., Int. Ed.* **2021**, *60*, 18930–18949.
- (4) Yang, Y.; Li, L.; Lin, R. B.; Ye, Y.; Yao, Z.; Yang, L.; Xiang, F.; Chen, S.; Zhang, Z.; Xiang, S.; Chen, B. Ethylene/ethane separation in a stable hydrogen-bonded organic framework through a gating mechanism. *Nat. Chem.* **2021**, *13*, 933–939.
- (5) Stang, P. J.; Diederich, F. *Modern acetylene chemistry*; VCH: 1995.
- (6) Guo, C. J.; Shen, D.; Bülow, M. 18-O-03 - Kinetic separation of binary mixtures of carbon dioxide and C₂ hydrocarbons on modified LTA-type zeolites. *Stud. Surf. Sci. Catal.* **2001**, *135*, 144.
- (7) Reid, C. R.; Thomas, K. M. Adsorption Kinetics and Size Exclusion Properties of Probe Molecules for the Selective Porosity in a Carbon Molecular Sieve Used for Air Separation. *J. Phys. Chem. B* **2001**, *105*, 10619–10629.
- (8) Matsuda, R.; Kitaura, R.; Kitagawa, S.; Kubota, Y.; Belosludov, R. V.; Kobayashi, T. C.; Sakamoto, H.; Chiba, T.; Takata, M.; Kawazoe, Y.; Mita, Y. Highly controlled acetylene accommodation in a metal-organic microporous material. *Nature* **2005**, *436*, 238–241.
- (9) Ye, Y.; Chen, S.; Chen, L.; Huang, J.; Ma, Z.; Li, Z.; Yao, Z.; Zhang, J.; Zhang, Z.; Xiang, S. Additive-Induced Supramolecular Isomerism and Enhancement of Robustness in Co(II)-Based MOFs for Efficiently Trapping Acetylene from Acetylene-Containing Mixtures. *ACS Appl. Mater. Interfaces* **2018**, *10*, 30912–30918.
- (10) Niu, Z.; Cui, X.; Pham, T.; Verma, G.; Lan, P. C.; Shan, C.; Xing, H.; Forrest, K. A.; Suepaul, S.; Space, B.; Nafady, A.; Al-Enizi, A. M.; Ma, S. A MOF-based Ultra-Strong Acetylene Nano-trap for Highly Efficient C₂H₂/CO₂ Separation. *Angew. Chem., Int. Ed.* **2021**, *60*, 5283–5288.
- (11) Chu, S.; Cui, Y.; Liu, N. The path towards sustainable energy. *Nat. Mater.* **2017**, *16*, 16–22.
- (12) Sircar, S. Pressure Swing Adsorption. *Ind. Eng. Chem. Res.* **2002**, *41*, 1389–1392.
- (13) Mason, J. A.; Sumida, K.; Herm, Z. R.; Krishna, R.; Long, J. R. Evaluating metal-organic frameworks for post-combustion carbon dioxide capture via temperature swing adsorption. *Energy Environ. Sci.* **2011**, *4*, 3030–3040.
- (14) Ye, Y.; Ma, Z.; Chen, L.; Lin, H.; Lin, Q.; Liu, L.; Li, Z.; Chen, S.; Zhang, Z.; Xiang, S. Microporous metal-organic frameworks with open metal sites and π -Lewis acidic pore surfaces for recovering ethylene from polyethylene off-gas. *J. Mater. Chem. A* **2018**, *6*, 20822–20828.
- (15) Qian, Q.; Asinger, P. A.; Lee, M. J.; Han, G.; Mizrahi Rodriguez, K.; Lin, S.; Benedetti, F. M.; Wu, A. X.; Chi, W. S.; Smith, Z. P. MOF-Based Membranes for Gas Separations. *Chem. Rev.* **2020**, *120*, 8161–8266.
- (16) Sholl, D. S.; Lively, R. P. Seven chemical separations to change the world. *Nature* **2016**, *532*, 435–437.
- (17) Furukawa, H.; Cordova, K. E.; O’Keeffe, M.; Yaghi, O. M. The chemistry and applications of metal-organic frameworks. *Science* **2013**, *341*, 1230444.
- (18) Zhao, X.; Wang, Y.; Li, D. S.; Bu, X.; Feng, P. Metal-Organic Frameworks for Separation. *Adv. Mater.* **2018**, *30*, 1705189.
- (19) Li, H.; Li, L.; Lin, R.-B.; Zhou, W.; Zhang, Z.; Xiang, S.; Chen, B. Porous metal-organic frameworks for gas storage and separation: Status and challenges. *EnergyChem* **2019**, *1*, 100006.
- (20) Wang, H.; Liu, Y.; Li, J. Designer Metal-Organic Frameworks for Size-Exclusion-Based Hydrocarbon Separations: Progress and Challenges. *Adv. Mater.* **2020**, *32*, 2002603.
- (21) Ye, Y.; Gong, L.; Xiang, S.; Zhang, Z.; Chen, B. Metal-Organic Frameworks as a Versatile Platform for Proton Conductors. *Adv. Mater.* **2020**, *32*, 1907090.
- (22) Vaidhyanathan, R.; Iremonger, S. S.; Shimizu, G. K.; Boyd, P. G.; Alavi, S.; Woo, T. K. Direct observation and quantification of CO₂ binding within an amine-functionalized nanoporous solid. *Science* **2010**, *330*, 650–653.
- (23) Lin, R. B.; Zhang, Z.; Chen, B. Achieving High Performance Metal-Organic Framework Materials through Pore Engineering. *Acc. Chem. Res.* **2021**, *54*, 3362–3376.
- (24) Bereciartua, P. J.; Cantin, A.; Corma, A.; Jorda, J. L.; Palomino, M.; Rey, F.; Valencia, S.; Corcoran, E. W., Jr.; Kortunov, P.; Ravikovitch, P. I.; Burton, A.; Yoon, C.; Wang, Y.; Paur, C.; Guzman, J.; Bishop, A. R.; Casty, G. L. Control of zeolite framework flexibility and pore topology for separation of ethane and ethylene. *Science* **2017**, *358*, 1068–1071.
- (25) Sevilla, M.; Fuertes, A. B. Sustainable porous carbons with a superior performance for CO₂ capture. *Energy Environ. Sci.* **2011**, *4*, 1765–1771.
- (26) Chen, Z.; Li, P.; Anderson, R.; Wang, X.; Zhang, X.; Robison, L.; Redfern, L. R.; Moribe, S.; Islamoglu, T.; Gomez-Gualdrón, D. A.; Yildirim, T.; Stoddart, J. F.; Farha, O. K. Balancing volumetric and gravimetric uptake in highly porous materials for clean energy. *Science* **2020**, *368*, 297–303.
- (27) Chen, Z.; Jiang, H.; Li, M.; O’Keeffe, M.; Eddaoudi, M. Reticular Chemistry 3.2: Typical Minimal Edge-Transitive Derived and Related Nets for the Design and Synthesis of Metal-Organic Frameworks. *Chem. Rev.* **2020**, *120*, 8039–8065.
- (28) Kim, E. J.; Siegelman, R. L.; Jiang, H. Z. H.; Forse, A. C.; Lee, J.-H.; Martell, J. D.; Milner, P. J.; Falkowski, J. M.; Neaton, J. B.; Reimer, J. A.; Weston, S. C.; Long, J. R. Cooperative carbon capture and steam regeneration with tetraamine-appended metal-organic frameworks. *Science* **2020**, *369*, 392–396.
- (29) Liao, P. Q.; Huang, N. Y.; Zhang, W. X.; Zhang, J. P.; Chen, X. M. Controlling guest conformation for efficient purification of butadiene. *Science* **2017**, *356*, 1193–1196.
- (30) Li, L.; Lin, R. B.; Krishna, R.; Li, H.; Xiang, S.; Wu, H.; Li, J.; Zhou, W.; Chen, B. Ethane/ethylene separation in a metal-organic framework with iron-peroxo sites. *Science* **2018**, *362*, 443–446.
- (31) Lin, R. B.; Li, L.; Zhou, H. L.; Wu, H.; He, C.; Li, S.; Krishna, R.; Li, J.; Zhou, W.; Chen, B. Molecular sieving of ethylene from ethane using a rigid metal-organic framework. *Nat. Mater.* **2018**, *17*, 1128–1133.
- (32) Wang, H.; Dong, X.; Colombo, V.; Wang, Q.; Liu, Y.; Liu, W.; Wang, X. L.; Huang, X. Y.; Proserpio, D. M.; Sironi, A.; Han, Y.; Li, J. Tailor-Made Microporous Metal-Organic Frameworks for the Full Separation of Propane from Propylene Through Selective Size Exclusion. *Adv. Mater.* **2018**, *30*, 1805088.
- (33) Gu, C.; Hosono, N.; Zheng, J. J.; Sato, Y.; Kusaka, S.; Sakaki, S.; Kitagawa, S. Design and control of gas diffusion process in a nanoporous soft crystal. *Science* **2019**, *363*, 387–391.
- (34) Chen, K. J.; Madden, D. G.; Mukherjee, S.; Pham, T.; Forrest, K. A.; Kumar, A.; Space, B.; Kong, J.; Zhang, Q. Y.; Zaworotko, M. J. Synergistic sorbent separation for one-step ethylene purification from a four-component mixture. *Science* **2019**, *366*, 241–246.
- (35) Liang, B.; Zhang, X.; Xie, Y.; Lin, R. B.; Krishna, R.; Cui, H.; Li, Z.; Shi, Y.; Wu, H.; Zhou, W.; Chen, B. An Ultramicroporous Metal-Organic Framework for High Sieving Separation of Propylene from Propane. *J. Am. Chem. Soc.* **2020**, *142*, 17795–17801.
- (36) Xiang, S.; Zhou, W.; Gallegos, J. M.; Liu, Y.; Chen, B. Exceptionally High Acetylene Uptake in a Microporous Metal-Organic Framework with Open Metal Sites. *J. Am. Chem. Soc.* **2009**, *131*, 12415–12419.
- (37) He, Y. B.; Krishna, R.; Chen, B. L. Metal-organic frameworks with potential for energy-efficient adsorptive separation of light hydrocarbons. *Energy Environ. Sci.* **2012**, *5*, 9107–9120.
- (38) Moreau, F.; da Silva, I.; Al Smail, N. H.; Easun, T. L.; Savage, M.; Godfrey, H. G.; Parker, S. F.; Manuel, P.; Yang, S.; Schroder, M. Unravelling exceptional acetylene and carbon dioxide adsorption

- within a tetra-amide functionalized metal-organic framework. *Nat. Commun.* **2017**, *8*, 14085.
- (39) Di, Z.; Liu, C.; Pang, J.; Chen, C.; Hu, F.; Yuan, D.; Wu, M.; Hong, M. Cage-Like Porous Materials with Simultaneous High C₂H₂ Storage and Excellent C₂H₂/CO₂ Separation Performance. *Angew. Chem., Int. Ed.* **2021**, *60*, 10828–10832.
- (40) Scott, H. S.; Shivanna, M.; Bajpai, A.; Madden, D. G.; Chen, K. J.; Pham, T.; Forrest, K. A.; Hogan, A.; Space, B.; Perry, J. J., IV; Zaworotko, M. J. Highly Selective Separation of C₂H₂ from CO₂ by a New Dichromate-Based Hybrid Ultramicroporous Material. *ACS Appl. Mater. Interfaces* **2017**, *9*, 33395–33400.
- (41) Lin, R. B.; Li, L.; Wu, H.; Arman, H.; Li, B.; Lin, R. G.; Zhou, W.; Chen, B. Optimized Separation of Acetylene from Carbon Dioxide and Ethylene in a Microporous Material. *J. Am. Chem. Soc.* **2017**, *139*, 8022–8028.
- (42) Zhang, L.; Jiang, K.; Yang, L.; Li, L.; Hu, E.; Yang, L.; Shao, K.; Xing, H.; Cui, Y.; Yang, Y.; Li, B.; Chen, B.; Qian, G. Benchmark C₂H₂ /CO₂ Separation in an Ultra-Microporous Metal-Organic Framework via Copper(I)-Alkynyl Chemistry. *Angew. Chem., Int. Ed.* **2021**, *60*, 15995–16002.
- (43) Yang, L.; Yan, L.; Wang, Y.; Liu, Z.; He, J.; Fu, Q.; Liu, D.; Gu, X.; Dai, P.; Li, L.; Zhao, X. Adsorption Site Selective Occupation Strategy within a Metal-Organic Framework for Highly Efficient Sieving Acetylene from Carbon Dioxide. *Angew. Chem., Int. Ed.* **2021**, *60*, 4570–4574.
- (44) Li, B.; Cui, X.; O’Nolan, D.; Wen, H. M.; Jiang, M.; Krishna, R.; Wu, H.; Lin, R. B.; Chen, Y. S.; Yuan, D.; Xing, H.; Zhou, W.; Ren, Q.; Qian, G.; Zaworotko, M. J.; Chen, B. An Ideal Molecular Sieve for Acetylene Removal from Ethylene with Record Selectivity and Productivity. *Adv. Mater.* **2017**, *29*, 1704210.
- (45) Chen, K. J.; Madden, D. G.; Pham, T.; Forrest, K. A.; Kumar, A.; Yang, Q. Y.; Xue, W.; Space, B.; Perry, J. J. t.; Zhang, J. P.; Chen, X. M.; Zaworotko, M. J. Tuning Pore Size in Square-Lattice Coordination Networks for Size-Selective Sieving of CO₂. *Angew. Chem., Int. Ed.* **2016**, *55*, 10268–10272.
- (46) Graham, C.; Pierrus, J.; Raab, R. E. Measurement of the electric quadrupole moments of CO₂, CO and N₂. *Mol. Phys.* **1989**, *67*, 939–955.
- (47) Halkier, A.; Coriani, S. On the molecular electric quadrupole moment of C₂H₂. *Chem. Phys. Lett.* **1999**, *303*, 408–412.
- (48) Pedersen, C. J. Cyclic polyethers and their complexes with metal salts. *J. Am. Chem. Soc.* **1967**, *89*, 7017–7036.
- (49) Escobar, L.; Ballester, P. Molecular Recognition in Water Using Macrocyclic Synthetic Receptors. *Chem. Rev.* **2021**, *121*, 2445–2514.
- (50) Liu, W.; Oliver, A. G.; Smith, B. D. Macrocyclic Receptor for Precious Gold, Platinum, or Palladium Coordination Complexes. *J. Am. Chem. Soc.* **2018**, *140*, 6810–6813.
- (51) Yang, L.; Cui, X.; Yang, Q.; Qian, S.; Wu, H.; Bao, Z.; Zhang, Z.; Ren, Q.; Zhou, W.; Chen, B.; Xing, H. A Single-Molecule Propyne Trap: Highly Efficient Removal of Propyne from Propylene with Anion-Pillared Ultramicroporous Materials. *Adv. Mater.* **2018**, *30*, 1705374.
- (52) Cadiau, A.; Lee, J. S.; Damasceno Borges, D.; Fabry, P.; Devic, T.; Wharmby, M. T.; Martineau, C.; Foucher, D.; Taulelle, F.; Jun, C. H.; Hwang, Y. K.; Stock, N.; De Lange, M. F.; Kapteijn, F.; Gascon, J.; Maurin, G.; Chang, J. S.; Serre, C. Design of hydrophilic metal organic framework water adsorbents for heat reallocation. *Adv. Mater.* **2015**, *27*, 4775–4780.
- (53) Reinsch, H.; van der Veen, M. A.; Gil, B.; Marszalek, B.; Verbiest, T.; de Vos, D.; Stock, N. Structures, Sorption Characteristics, and Nonlinear Optical Properties of a New Series of Highly Stable Aluminum MOFs. *Chem. Mater.* **2013**, *25*, 17–26.
- (54) Lenzen, D.; Zhao, J.; Ernst, S. J.; Wahiduzzaman, M.; Ken Inge, A.; Frohlich, D.; Xu, H.; Bart, H. J.; Janiak, C.; Henninger, S.; Maurin, G.; Zou, X.; Stock, N. A metal-organic framework for efficient water-based ultra-low-temperature-driven cooling. *Nat. Commun.* **2019**, *10*, 3025.
- (55) Millange, F.; Serre, C.; Ferey, G. Synthesis, structure determination and properties of MIL-53as and MIL-53ht: the first CrIII hybrid inorganic-organic microporous solids: Cr^{III}(OH)₂(O₂C-C₆H₄-CO₂)₂(HO₂C-C₆H₄-CO₂H)_x. *Chem. Commun.* **2002**, 822–823.
- (56) Li, H.; Liu, C.; Chen, C.; Di, Z.; Yuan, D.; Pang, J.; Wei, W.; Wu, M.; Hong, M. An Unprecedented Pillar-Cage Fluorinated Hybrid Porous Framework with Highly Efficient Acetylene Storage and Separation. *Angew. Chem., Int. Ed.* **2021**, *60*, 7547–7552.
- (57) Ye, Y.; Ma, Z.; Lin, R.-B.; Krishna, R.; Zhou, W.; Lin, Q.; Zhang, Z.; Xiang, S.; Chen, B. Pore Space Partition within a Metal-Organic Framework for Highly Efficient C₂H₂/CO₂ Separation. *J. Am. Chem. Soc.* **2019**, *141*, 4130–4136.
- (58) Luo, F.; Yan, C.; Dang, L.; Krishna, R.; Zhou, W.; Wu, H.; Dong, X.; Han, Y.; Hu, T. L.; O’Keeffe, M.; Wang, L.; Luo, M.; Lin, R. B.; Chen, B. UTSA-74: A MOF-74 Isomer with Two Accessible Binding Sites per Metal Center for Highly Selective Gas Separation. *J. Am. Chem. Soc.* **2016**, *138*, 5678–5684.
- (59) Gao, J.; Qian, X.; Lin, R. B.; Krishna, R.; Wu, H.; Zhou, W.; Chen, B. Mixed Metal-Organic Framework with Multiple Binding Sites for Efficient C₂H₂/CO₂ Separation. *Angew. Chem., Int. Ed.* **2020**, *59*, 4396–4400.
- (60) Liu, S.; Han, X.; Chai, Y.; Wu, G.; Li, W.; Li, J.; da Silva, I.; Manuel, P.; Cheng, Y.; Daemen, L. L.; Ramirez-Cuesta, A. J.; Shi, W.; Guan, N.; Yang, S.; Li, L. Efficient Separation of Acetylene and Carbon Dioxide in a Decorated Zeolite. *Angew. Chem., Int. Ed.* **2021**, *60*, 6526–6532.
- (61) Pang, J.; Jiang, F.; Wu, M.; Liu, C.; Su, K.; Lu, W.; Yuan, D.; Hong, M. A porous metal-organic framework with ultrahigh acetylene uptake capacity under ambient conditions. *Nat. Commun.* **2015**, *6*, 7575.
- (62) Xiang, S.; Zhou, W.; Zhang, Z.; Green, M. A.; Liu, Y.; Chen, B. Open metal sites within isostructural metal-organic frameworks for differential recognition of acetylene and extraordinarily high acetylene storage capacity at room temperature. *Angew. Chem., Int. Ed.* **2010**, *49*, 4615–4618.
- (63) McIntosh, D. The Physical Properties of Liquid and Solid Acetylene. *J. Phys. Chem.* **1907**, *11*, 306–317.
- (64) Myers, A. L.; Prausnitz, J. M. Thermodynamics of mixed-gas adsorption. *AIChE J.* **1965**, *11*, 121–127.
- (65) Qazvini, O. T.; Babarao, R.; Telfer, S. G. Multipurpose Metal-Organic Framework for the Adsorption of Acetylene: Ethylene Purification and Carbon Dioxide Removal. *Chem. Mater.* **2019**, *31*, 4919–4926.
- (66) Kumar, N.; Mukherjee, S.; Harvey-Reid, N. C.; Bezrukov, A. A.; Tan, K.; Martins, V.; Vandichel, M.; Pham, T.; van Wyk, L. M.; Oyekan, K.; Kumar, A.; Forrest, K. A.; Patil, K. M.; Barbour, L. J.; Space, B.; Huang, Y.; Kruger, P. E.; Zaworotko, M. J. Breaking the trade-off between selectivity and adsorption capacity for gas separation. *Chem* **2021**, *7*, 3085–3098.
- (67) Chen, K. J.; Scott, H. S.; Madden, D. G.; Pham, T.; Kumar, A.; Bajpai, A.; Lusi, M.; Forrest, K. A.; Space, B.; Perry, J. J.; Zaworotko, M. J. Benchmark C₂H₂/CO₂ and CO₂/C₂H₂ Separation by Two Closely Related Hybrid Ultramicroporous Materials. *Chem* **2016**, *1*, 753–765.
- (68) Li, P.; He, Y.; Zhao, Y.; Weng, L.; Wang, H.; Krishna, R.; Wu, H.; Zhou, W.; O’Keeffe, M.; Han, Y.; Chen, B. A rod-packing microporous hydrogen-bonded organic framework for highly selective separation of C₂H₂/CO₂ at room temperature. *Angew. Chem., Int. Ed.* **2015**, *54*, 574–577.
- (69) Cui, X.; Chen, K.; Xing, H.; Yang, Q.; Krishna, R.; Bao, Z.; Wu, H.; Zhou, W.; Dong, X.; Han, Y.; Li, B.; Ren, Q.; Zaworotko, M. J.; Chen, B. Pore chemistry and size control in hybrid porous materials for acetylene capture from ethylene. *Science* **2016**, *353*, 141–144.
- (70) Gong, W.; Cui, H.; Xie, Y.; Li, Y.; Tang, X.; Liu, Y.; Cui, Y.; Chen, B. Efficient C₂H₂/CO₂ Separation in Ultramicroporous Metal-Organic Frameworks with Record C₂H₂ Storage Density. *J. Am. Chem. Soc.* **2021**, *143*, 14869–14876.
- (71) Yang, S.; Ramirez-Cuesta, A. J.; Newby, R.; Garcia-Sakai, V.; Manuel, P.; Callear, S. K.; Campbell, S. I.; Tang, C. C.; Schröder, M. Supramolecular binding and separation of hydrocarbons within a

functionalized porous metal–organic framework. *Nat. Chem.* **2015**, *7*, 121–129.

(72) Pei, J.; Wen, H. M.; Gu, X. W.; Qian, Q. L.; Yang, Y.; Cui, Y.; Li, B.; Chen, B.; Qian, G. Dense Packing of Acetylene in a Stable and Low-Cost Metal-Organic Framework for Efficient C₂H₂/CO₂ Separation. *Angew. Chem., Int. Ed.* **2021**, *60*, 25068–25074.

(73) Pei, J.; Shao, K.; Wang, J. X.; Wen, H. M.; Yang, Y.; Cui, Y.; Krishna, R.; Li, B.; Qian, G. A Chemically Stable Hofmann-Type Metal-Organic Framework with Sandwich-Like Binding Sites for Benchmark Acetylene Capture. *Adv. Mater.* **2020**, *32*, 1908275.

(74) Krishna, R. Metrics for Evaluation and Screening of Metal–Organic Frameworks for Applications in Mixture Separations. *ACS Omega* **2020**, *5*, 16987–17004.

(75) Krishna, R. Screening metal–organic frameworks for mixture separations in fixed-bed adsorbers using a combined selectivity/capacity metric. *RSC Adv.* **2017**, *7*, 35724–35737.

(76) Krishna, R. Methodologies for screening and selection of crystalline microporous materials in mixture separations. *Sep. Purif. Technol.* **2018**, *194*, 281–300.

(77) Zhang, Y.; Hu, J.; Krishna, R.; Wang, L.; Yang, L.; Cui, X.; Duttwyler, S.; Xing, H. Rational Design of Microporous MOFs with Anionic Boron Cluster Functionality and Cooperative Dihydrogen Binding Sites for Highly Selective Capture of Acetylene. *Angew. Chem., Int. Ed.* **2020**, *59*, 17664–17669.

(78) Wang, L.; Sun, W.; Zhang, Y.; Xu, N.; Krishna, R.; Hu, J.; Jiang, Y.; He, Y.; Xing, H. Interpenetration Symmetry Control Within Ultramicroporous Robust Boron Cluster Hybrid MOFs for Benchmark Purification of Acetylene from Carbon Dioxide. *Angew. Chem., Int. Ed.* **2021**, *60*, 22865–22870.

(79) Nijem, N.; Wu, H.; Canepa, P.; Marti, A.; Balkus, K. J., Jr.; Thonhauser, T.; Li, J.; Chabal, Y. J. Tuning the gate opening pressure of Metal-Organic Frameworks (MOFs) for the selective separation of hydrocarbons. *J. Am. Chem. Soc.* **2012**, *134*, 15201–15204.

(80) Mukherjee, S.; Kumar, N.; Bezrukov, A. A.; Tan, K.; Pham, T.; Forrest, K. A.; Oyekan, K. A.; Qazvini, O. T.; Madden, D. G.; Space, B.; Zaworotko, M. J. Amino-Functionalised Hybrid Ultramicroporous Materials that Enable Single-Step Ethylene Purification from a Ternary Mixture. *Angew. Chem., Int. Ed.* **2021**, *60*, 10902–10909.

(81) Maréchal, Y. *The Hydrogen Bond and the Water Molecule: The Physics and Chemistry of Water, Aqueous and Bio-Media*; Elsevier Science: 2007.

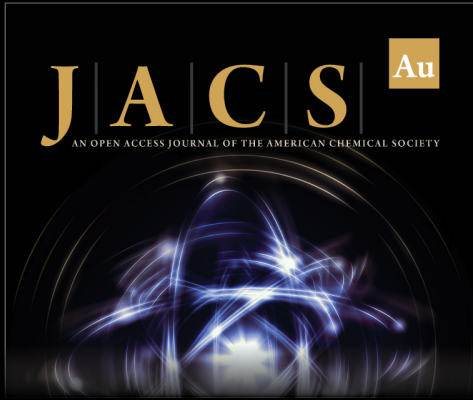
(82) Deacon, G. B.; Phillips, R. J. Relationships between the carbon-oxygen stretching frequencies of carboxylate complexes and the type of carboxylate coordination. *Coord. Chem. Rev.* **1980**, *33*, 227–250.

(83) Colthup, N. B.; Daly, L. H.; Wiberley, S. E. *Introduction to Infrared and Raman Spectroscopy*, 3rd ed.; Academic Press: 1990.

(84) Damasceno Borges, D.; Normand, P.; Permiakova, A.; Babarao, R.; Heymans, N.; Galvao, D. S.; Serre, C.; De Weireld, G.; Maurin, G. Gas Adsorption and Separation by the Al-Based Metal-Organic Framework MIL-160. *J. Phys. Chem. C* **2017**, *121*, 26822–26832.


(85) Henkelman, G.; Jónsson, H. Improved tangent estimate in the nudged elastic band method for finding minimum energy paths and saddle points. *J. Chem. Phys.* **2000**, *113*, 9978–9985.


(86) Henkelman, G.; Uberuaga, B. P.; Jónsson, H. A climbing image nudged elastic band method for finding saddle points and minimum energy paths. *J. Chem. Phys.* **2000**, *113*, 9901–9904.



JACS Au
AN OPEN ACCESS JOURNAL OF THE AMERICAN CHEMICAL SOCIETY

Editor-in-Chief
Prof. Christopher W. Jones
Georgia Institute of Technology, USA

Open for Submissions 

pubs.acs.org/jacsau  ACS Publications
Most Trusted. Most Cited. Most Read.

Supporting Information

Metal-Organic Framework based Hydrogen-Bonding Nanotrap for Efficient Acetylene Storage and Separation

Yingxiang Ye,^{1,#} Shikai Xian,^{2,3,#} Hui Cui,⁴ Kui Tan,⁵ Lingshan Gong,¹ Bin Liang,¹ Tony Pham,⁶ Haardik Pandey,⁷ Rajamani Krishna,⁸ Pui Ching Lan,¹ Katherine A. Forrest,⁶ Brian Space,⁹ Timo Thonhauser,⁷ Jing Li,^{2,*} and Shengqian Ma^{1,*}

¹Department of Chemistry, University of North Texas, Denton, Texas 76201, United States

²Department of Chemistry and Chemical Biology, Rutgers University, Piscataway, New Jersey 08854, United States

³Hoffmann Institute of Advanced Materials, Shenzhen Polytechnic, Shenzhen, Guangdong 518055, China

⁴Department of Chemistry, University of Texas at San Antonio, San Antonio, Texas 78249-0698, United States

⁵Department of Materials Science & Engineering, University of Texas at Dallas, Richardson, Texas 75080, United States

⁶Department of Chemistry, University of South Florida, Tampa, Florida 33620, United States

⁷Department of Physics and Center for Functional Materials, Wake Forest University, Winston-Salem, North Carolina 27109, United States

⁸Van 't Hoff Institute for Molecular Sciences, University of Amsterdam, 1098 XH Amsterdam, The Netherlands

⁹Department of Chemistry, North Carolina State University, Raleigh, North Carolina 27695, United States

[#]Y. Ye and S. Xian contributed equally to this work.

*Corresponding Authors, Jing Li, E-mail: jingli@rutgers.edu; Shengqian Ma, E-mail: Shengqian.Ma@unt.edu

Table of Contents

Experimental Section	S3
Table S1. Comparison of C ₂ H ₂ and CO ₂	S6
Figures S1-5. Supplementary structural figures.....	S6
Figures S6-8. FT-IR spectra of the as-synthesized samples.....	S9
Figures S9-11. Powder X-ray diffraction patterns.....	S10
Figures S12-14. The TGA curves of the as-synthesized samples.....	S11
Figures S15-27. Supplementary gas adsorption isotherms.....	S12
Figures S28-33. Single-site Langmuir-Freundlich equations fit for gas adsorption.....	S17
Figures S34-38. IAST calculations of mixture adsorption isotherms and selectivity.....	S20
Figure S39. Cycles of C ₂ H ₂ adsorption isotherms.....	S21
Table S2. Comparison of simulated C ₂ H ₂ /CO ₂ separation performances.....	S23
Figure S40. Transient breakthrough simulation curves.....	S24
Figures S41-44. Cycling breakthrough curves for gas mixture separation.....	S26
Table S3. Comparison of actual C ₂ H ₂ /CO ₂ separation performances.....	S27
Figure S45. Full IR difference spectra of CAU-23 and CAU-10H.....	S28
Table S4. Summary of selected vibrational modes associated with FDC linker.....	S29
Table S5. Calculated averaged total potential energies.....	S31
Figures S46-47. CMC-calculated binding sites and adsorption configurations.....	S32
Figure S48. Diffusion barrier energy and induced charge densities of CO ₂ and C ₂ H ₂	S35
Table S6. C ₂ H ₂ adsorption performances on some representative porous materials.....	S36
Supplementary References	S38

Experimental Section

Materials and Instrumentation. All reagents and solvents were used directly as received from the chemical supplier without further purification. Fourier-transform infrared spectra (FT-IR) were recorded on a PerkinElmer Spectrum One FT-IR instrument from 4000 to 400 cm^{-1} . The powder X-ray diffraction (PXRD) data were collected using a Bruker D8 Advance, Cu-K α radiation of 40 mA, 40 kV, $\lambda = 0.15418$ nm, 2θ scanning range of 5~50°, a scan step size of 0.02° and a time of 3 s per step. The simulated pattern was produced using the Mercury V1.4 program and reported cif file. The TA Instruments TGA Q50 was used to record thermal gravimetric analysis (TGA) data from room temperature to 800 °C at a heating rate of 10 °C/min under N₂ atmosphere.

Gas Adsorption Measurements. The single-component gas (C₂H₂, CO₂ and N₂) adsorption measurements were performed on an automatic volumetric adsorption apparatus Micromeritics ASAP 2020 HD88 surface area analyzer. Prior to the gas adsorption analyses, the as-synthesized samples were activated according to the reported procedure (see Experimental step for details). The experimental temperatures were controlled by liquid nitrogen bath (77 K), ice-water bath (273 K), and water bath (298 K), respectively.

Synthesis of MIL-160

MIL-160 was synthesized according to the literature.¹ Al(OH)(CH₃COO)₂ (7.5 mmol, 1.171 g) and 2,5-furandicarboxylic acid (7.5 mmol, 1.216 g) were added to a round-bottomed flask (100 mL) containing distilled water (25 mL). The mixture was then stirred under reflux for approximately 24 h. The resulting white solid was recovered by filtration, washed with ethanol, and dried in the oven at 100 °C. The phase purity of the as-synthesized sample was further confirmed by PXRD patterns. Prior to gas adsorption analyses, the sample was activated at 150 °C for 10 h under reduced pressure condition.

Synthesis of CAU-10H

CAU-10H was synthesized according to the reported procedure with slightly modification.² A mixture of Al(NO₃)₃·9H₂O (1.345 g, 3.59 mmol), isophthalic acid (0.595 g, 3.59 mmol) and acetonitrile (10 mL) were placed in a PTFE lined steel autoclave (20 mL). After that, the autoclave was heated at 130 °C oven for 1 day. After the reaction mixture cooled down to room temperature, the crude product (slightly yellowish solid) was obtained via filtration. For purification (removal of impurities), 1 g of crude product was stirred (400 rpm) in 50 mL of deionized water for 3 hours at room temperature, yielding 0.58 g of a white solid after filtration. The phase purity of CAU-10H was further confirmed by PXRD patterns. Prior to gas adsorption analyses, the purified sample was activated at 150 °C for 10 h under reduced pressure condition.

Synthesis of CAU-23

CAU-23 was synthesized according to the literature.³ 2,5-thiophenedicarboxylic acid (6.26 mmol, H₂TDC) was mixed with 12.75 mmol of NaOH and stirred in 25 mL de-ionized H₂O until a clear solution of Na₂TDC was achieved. After complete dissolution of H₂TDC, 1 eq. of Al³⁺ from two aqueous solutions of aluminum chloride hexahydrate (AlCl₃·6H₂O; 1.0 mol L⁻¹; 4.69 mL; 4.69 mmol) and sodium aluminate (NaAlO₂·0.2H₂O; 0.5 mol L⁻¹; 3.1 mL; 1.56 mmol) was added to the above linker solution. The resulting suspension was then stirred under reflux conditions for 6 h.

The cooled down suspension was centrifuged to recover a white product. The precipitate was dispersed three times in 45 mL each of de-ionized water and afterwards centrifuged. In a final step, the product was dispersed in 45 mL de-ionized water and stirred for at least 16 h before being centrifuged again. The resulting white solid was dried in a vacuum oven at 60 °C for not less than 24 h. The phase purity of the as-synthesized sample was confirmed by PXRD patterns. Prior to gas adsorption analyses, the sample was activated at 150 °C for 10 h under reduced pressure condition.

The isosteric heat of adsorption (Q_{st}): The isosteric heat of adsorption for C₂H₂ and CO₂ was calculated using the data collected at 273 and 298 K. The data were fitted first using a virial-type expression composed of parameters a_i and b_i (eq 1). Then, the Q_{st} (kJ mol⁻¹) was calculated from the fitting parameters using eq 2, where p is the pressure (mmHg), T is the temperature (K), R is the universal gas constant (8.314 J·mol⁻¹·K⁻¹), N is the amount adsorbed (mg g⁻¹), and m and n determine the number of terms required to adequately describe the isotherm.

$$\ln p = \ln N + \frac{1}{T} \sum_{i=0}^m a_i N_i + \sum_{i=0}^n b_i N_i \quad (1)$$

$$Q_{st} = -R \sum_{i=0}^m a_i N_i \quad (2)$$

Prediction of the Gas Adsorption Selectivity by IAST. The ideal adsorption solution theory (IAST)⁴ was used to predict the binary mixture adsorption from the experimental pure gas isotherms. To perform the integrations required by IAST, single-component isotherms should be fitted by the correct model. In practice, several methods are available; for this set of data we found that the single-site Langmuir-Freundlich equation was successful in fitting the results.

$$N = N^{\max} \times \frac{bp^{1/n}}{1+bp^{1/n}} \quad (3)$$

where p is the pressure of the bulk gas in equilibrium with the adsorbed phase (kPa), N is the amount adsorbed per mass of adsorbent (mmol g⁻¹), N^{\max} is the saturation capacities of site 1 (mmol g⁻¹), b is the affinity coefficients of site 1 (1/kPa) and n represents the deviations from an ideal homogeneous surface. The fitted parameters were then used to predict multi-component adsorption with IAST. The adsorption selectivity based on IAST for mixed C₂H₂/CO₂ is defined by the following equation:

$$S_{A/B} = \frac{x_A y_B}{x_B y_A} \quad (4)$$

where x_i and y_i are the mole fractions of component i ($i = A, B$) in the adsorbed and bulk phases, respectively.

Table S1. Comparison of C₂H₂ and CO₂

Gas molecules	Dynamic Size (Å)	Molecular size (Å ³)	Boiling point (K)	Quadrupole Moment (C·m ²)
C ₂ H ₂	3.3	3.32 × 3.34 × 5.70	189.3	20.5 × 10 ⁻⁴⁰
CO ₂	3.3	3.18 × 3.33 × 5.36	194.7	-13.4 × 10 ⁻⁴⁰

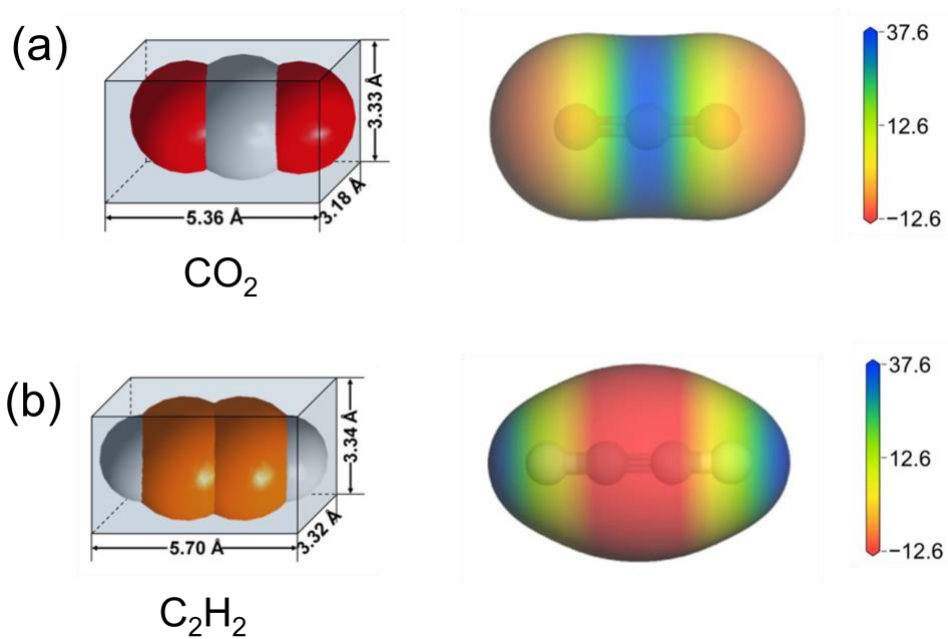


Figure S1. Comparison of molecular size and electrostatic potential difference of (a) CO₂ and (b) C₂H₂. The gradation on the scale bar is in kcal mol⁻¹. Reproduced with permission.⁵⁻⁶ Copyright 2021, Wiley-VCH.

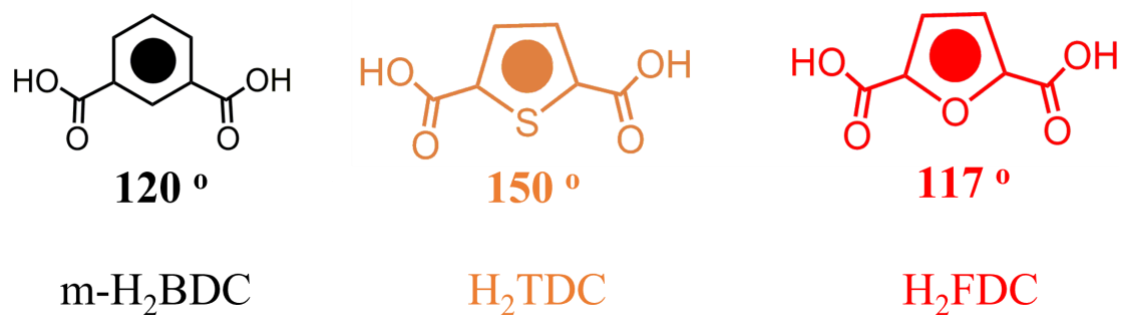


Figure S2. The organic linkers used in this work and their opening angles.

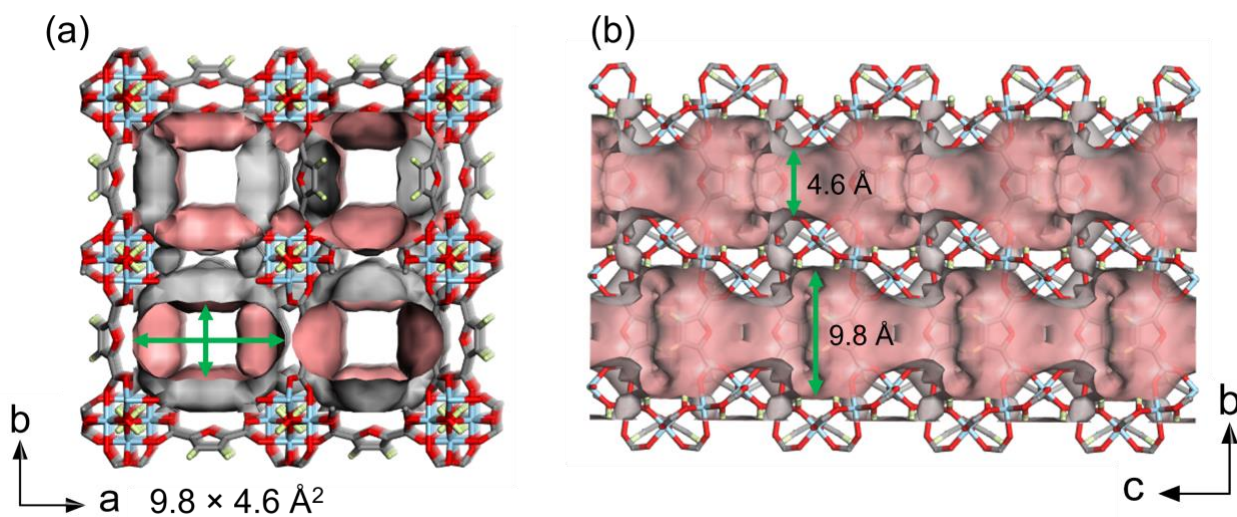


Figure S3. Accessible Connolly Surface calculated with the Connolly radius of 1.4 Å and the Grid interval of 0.25 Å for MIL-160. Grey represents the outside surface of the channel, and pink represents the inner surface.

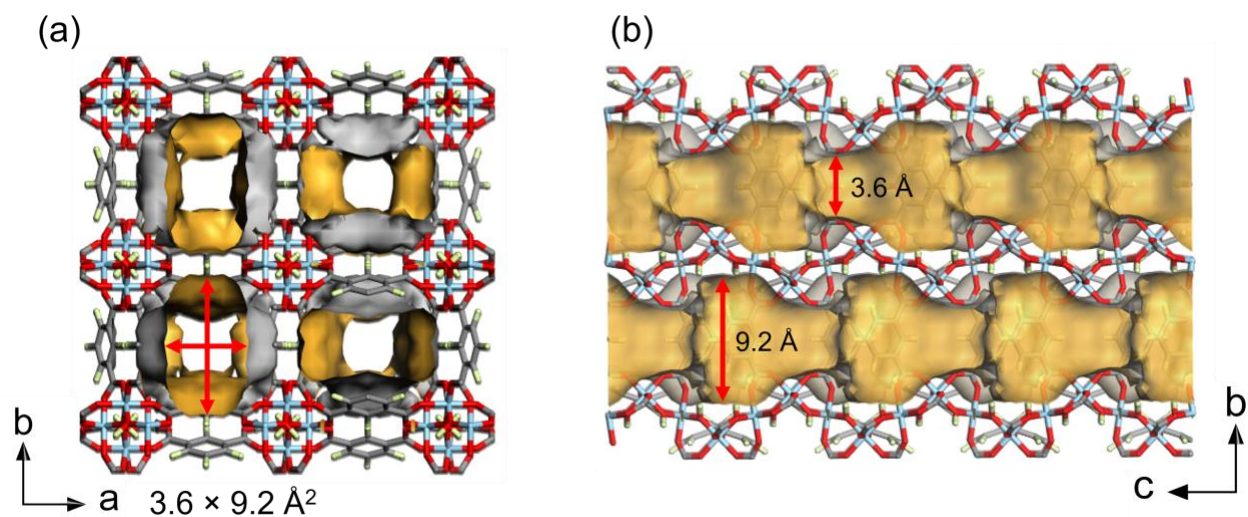


Figure S4. Accessible Connolly Surface calculated with the Connolly radius of 1.4 Å and the Grid interval of 0.25 Å for CAU-10H. Grey represents the outside surface of the channel, and khaki represents the inner surface.

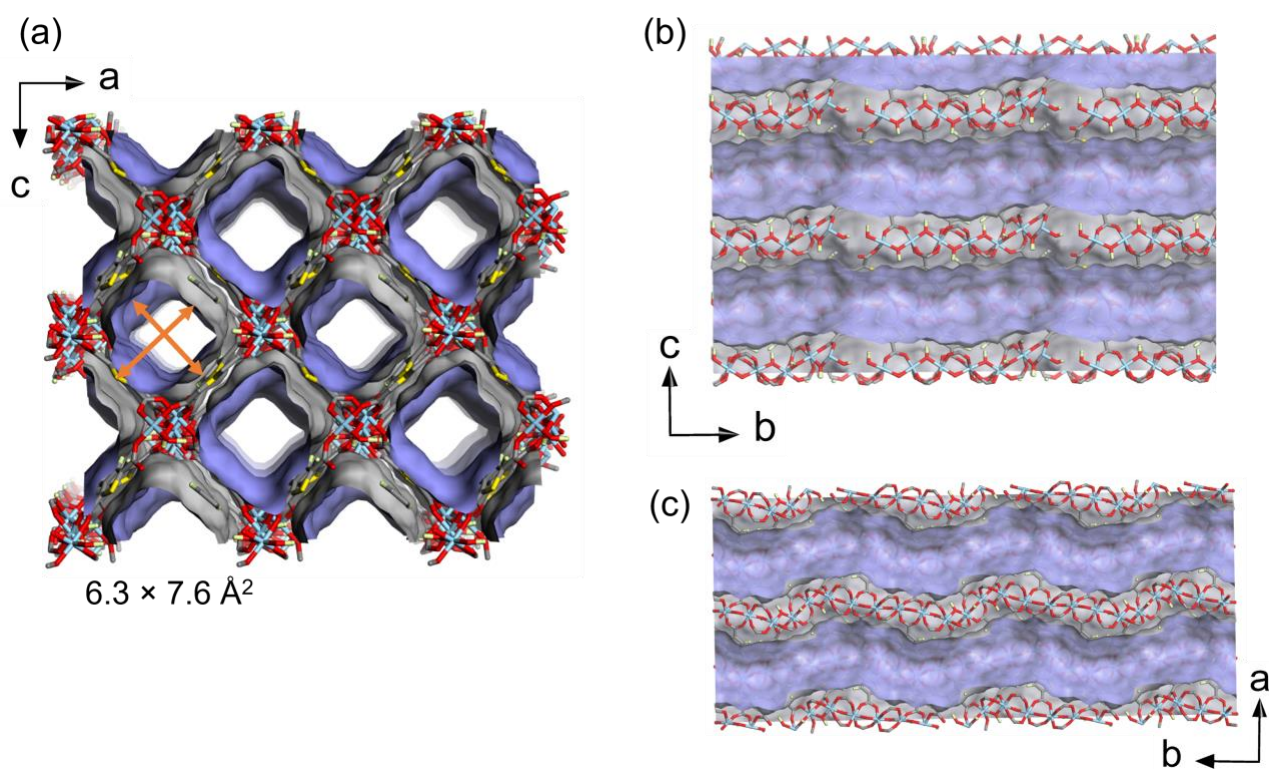


Figure S5. Accessible Connolly Surface calculated with the Connolly radius of 1.4 Å and the Grid interval of 0.25 Å for CAU-23. Grey represents the outside surface of the channel, and violet represents the inner surface.

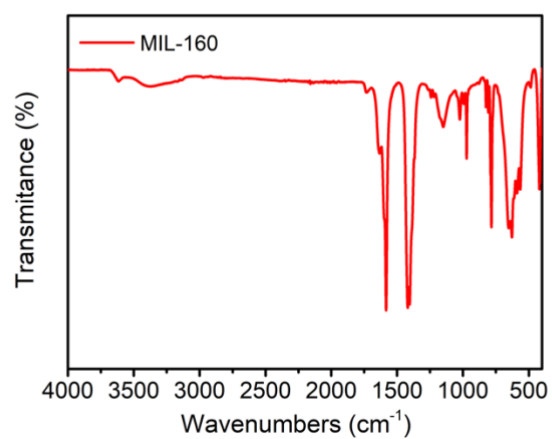


Figure S6. FT-IR spectrum of MIL-160.

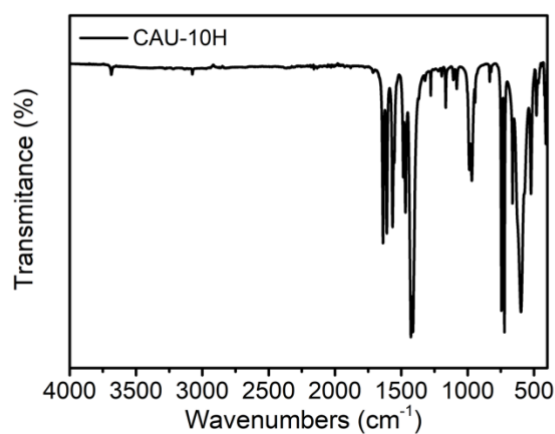


Figure S7. FT-IR spectrum of CAU-10H.

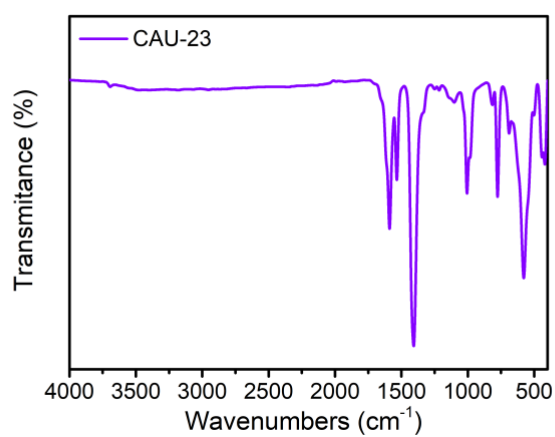


Figure S8. FT-IR spectrum of CAU-23.

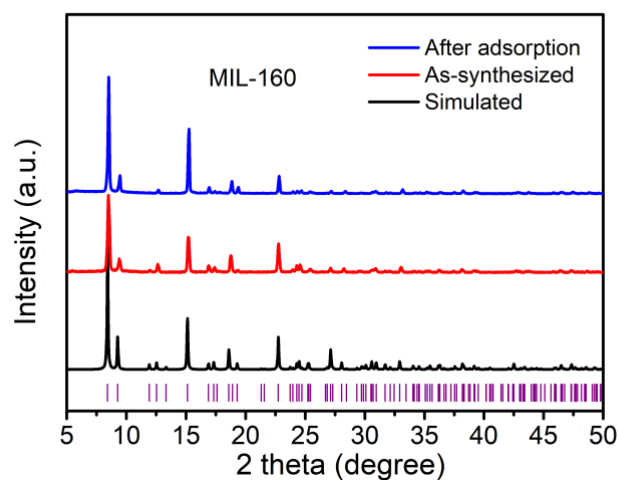


Figure S9. The powder X-ray diffraction patterns for MIL-160.

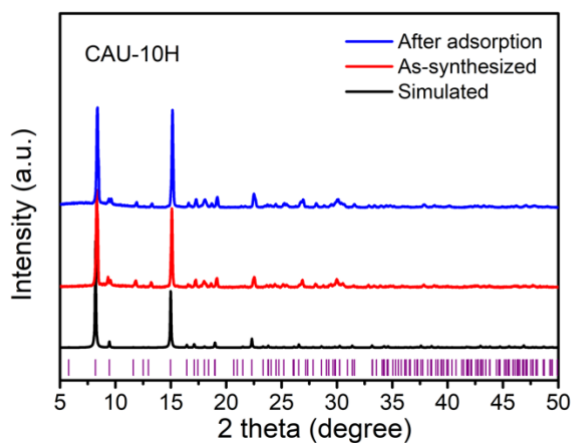


Figure S10. The powder X-ray diffraction patterns for CAU-10H.

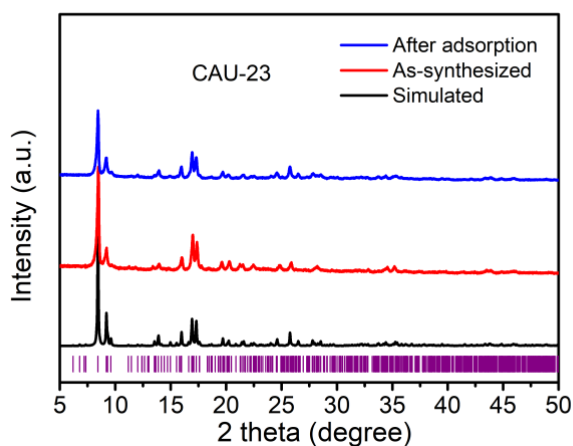


Figure S11. The powder X-ray diffraction patterns for CAU-23.

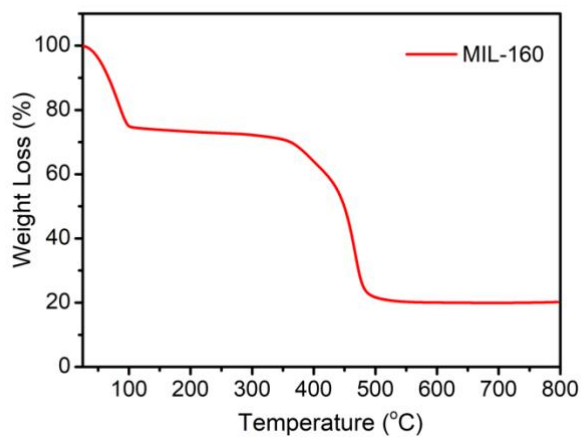


Figure S12. The TGA curve for MIL-160 under N₂ atmosphere with a heating rate of 10 K min⁻¹.

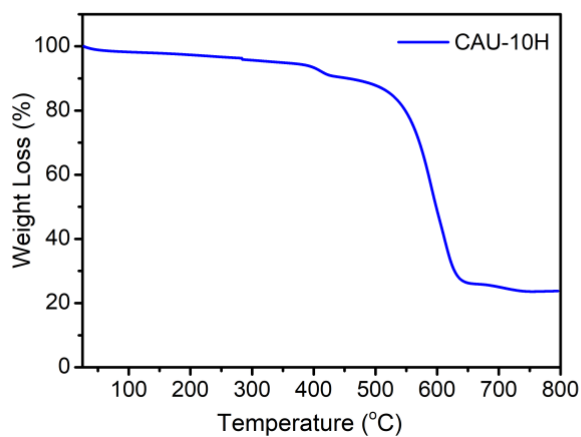


Figure S13. The TGA curve for CAU-10H under N₂ atmosphere with a heating rate of 10 K min⁻¹.

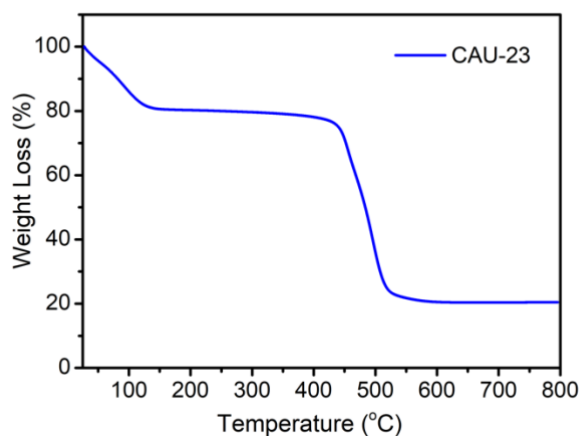


Figure S14. The TGA curve for CAU-23 under N₂ atmosphere with a heating rate of 10 K min⁻¹.

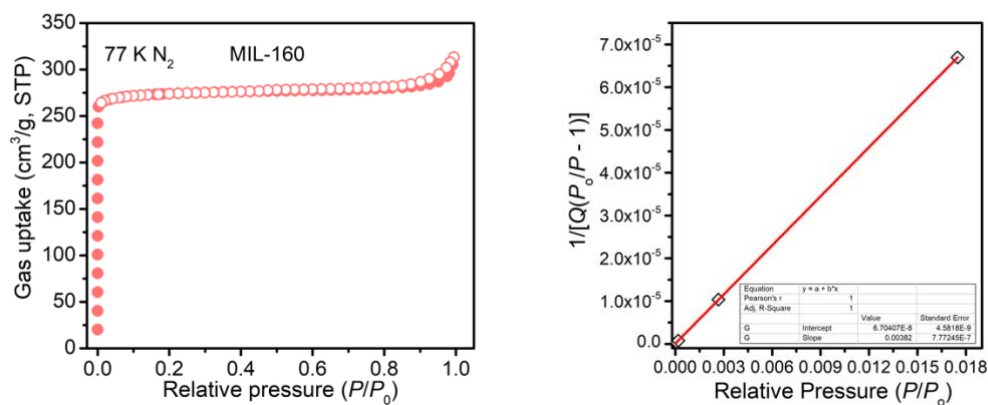


Figure S15. BET calculation for MIL-160 based on their corresponding N₂ adsorption isotherms at 77 K.

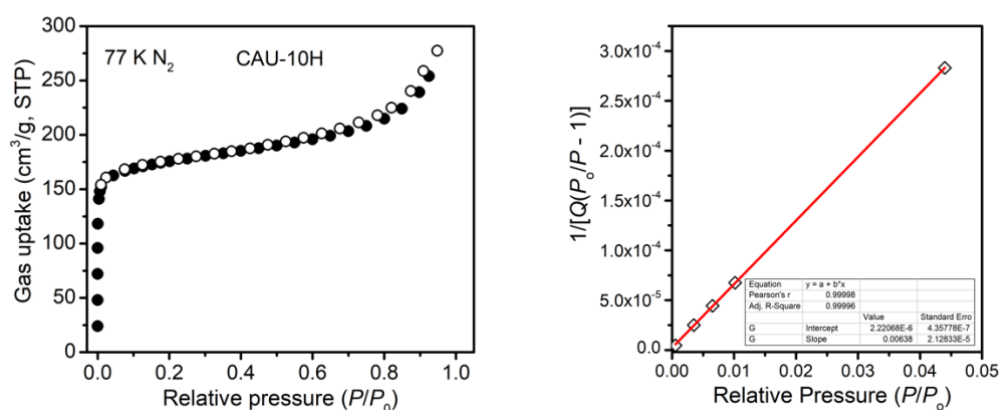


Figure S16. BET calculation for CAU-10H based on their corresponding N₂ adsorption isotherms at 77 K.

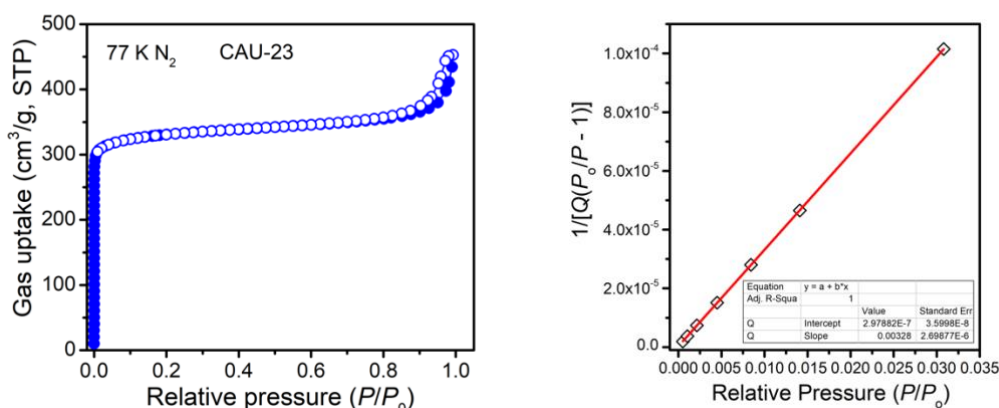


Figure S17. BET calculation for CAU-23 based on their corresponding N₂ adsorption isotherms at 77 K.

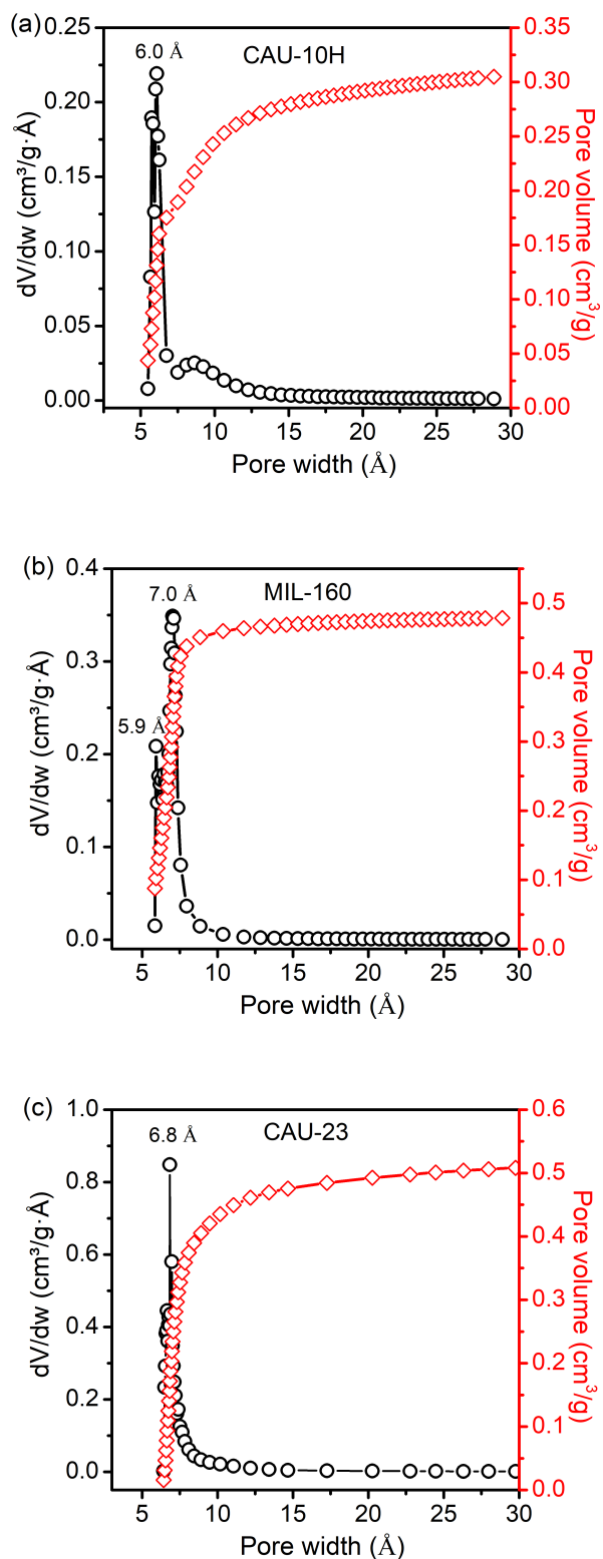


Figure S18. (a-c) Pore size distribution of CAU-10H, MIL-160, and CAU-23, calculated by 77 K N_2 isotherms based on the Horvath-Kawazoe cylinder model.

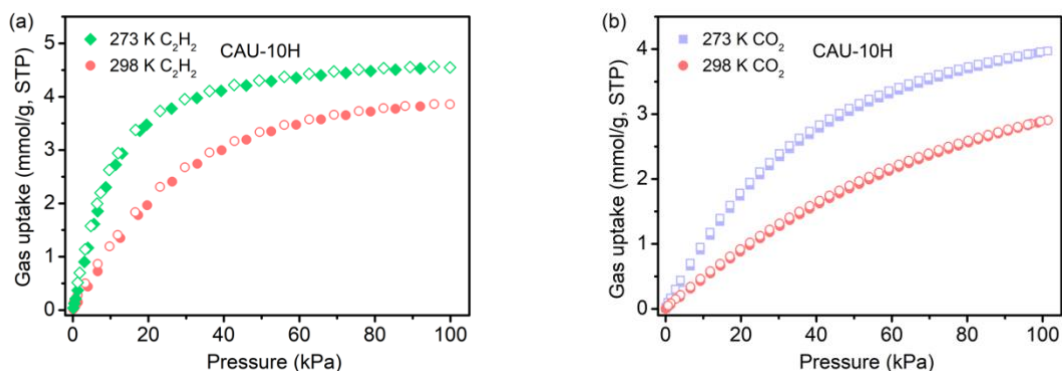


Figure S19. (a) C_2H_2 and (b) CO_2 adsorption isotherms for CAU-10H at 273 K and 298 K.

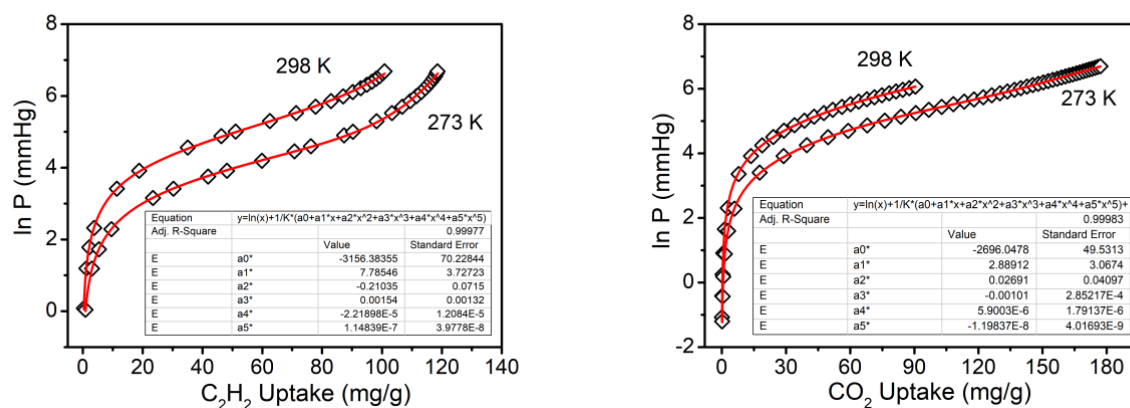


Figure S20. Experimental data (open symbol) and corresponding fittings (solid line) of C_2H_2 and CO_2 adsorption isotherms of CAU-10H at 273 K and 298 K. Fit curves are obtained by the virial-type expression.

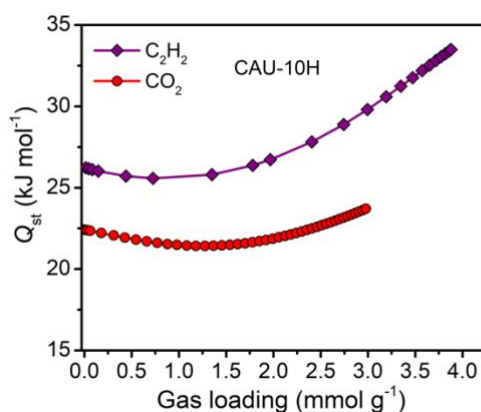


Figure S21. The heat of adsorption of CAU-10H for C_2H_2 and CO_2 .

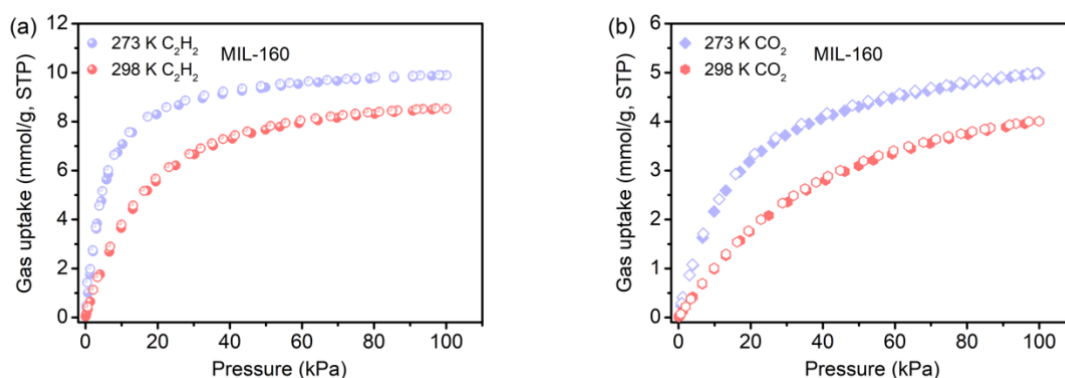


Figure S22. (a) C_2H_2 and (b) CO_2 adsorption isotherms for MIL-160 at 273 K and 298 K.

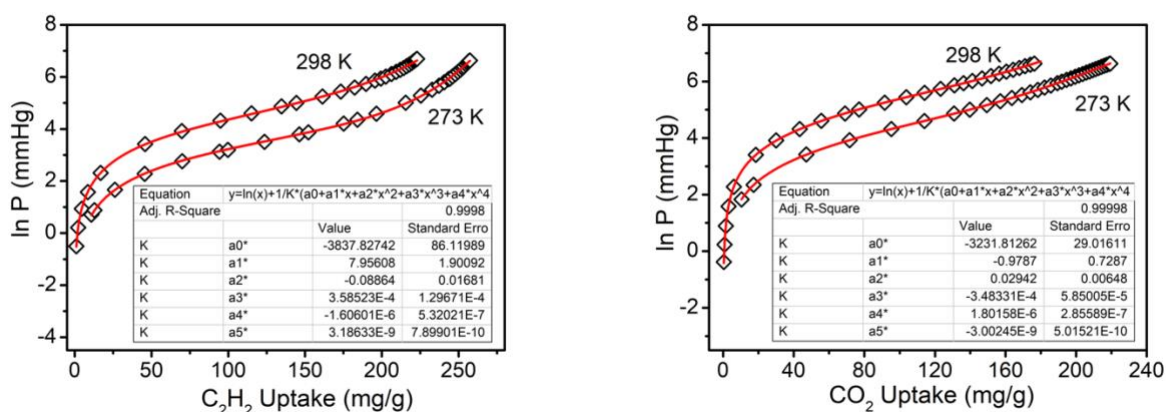


Figure S23. Experimental data (open symbol) and corresponding fittings (solid line) of C_2H_2 and CO_2 adsorption isotherms of MIL-160 at 273 K and 298 K. Fit curves are obtained by the virial-type expression.

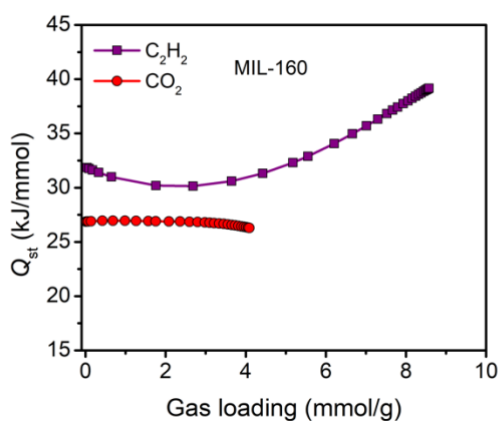


Figure S24. The heat of adsorption of MIL-160 for C_2H_2 and CO_2 .

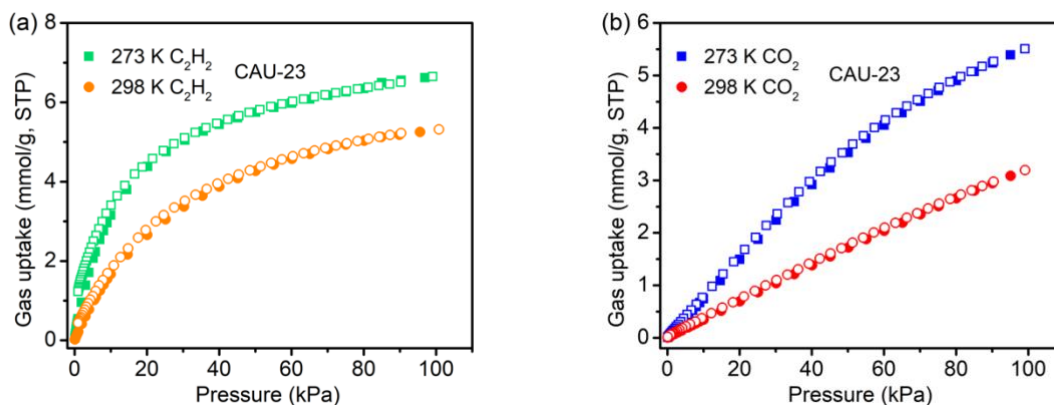


Figure S25. (a) C₂H₂ and (b) CO₂ adsorption isotherms for CAU-23 at 273 K and 298 K.

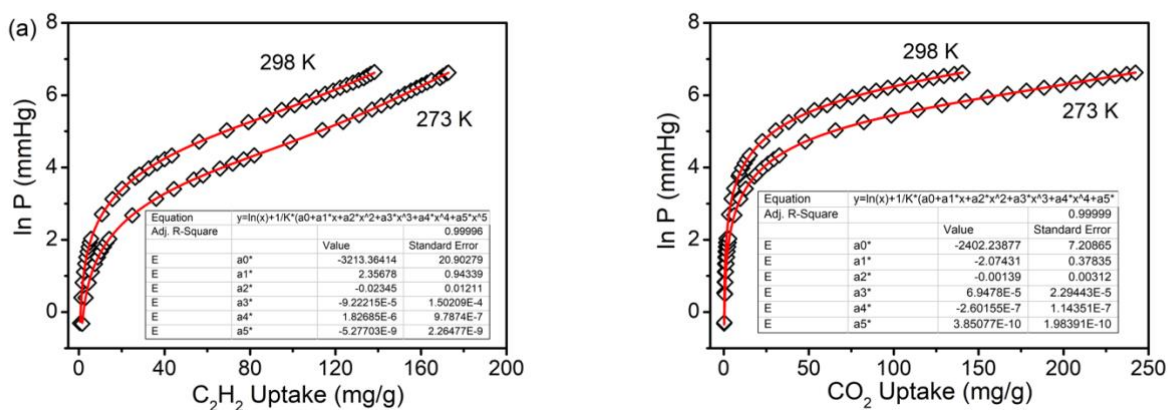


Figure S26. Experimental data (open symbol) and corresponding fittings (solid line) of C₂H₂ and CO₂ adsorption isotherms of CAU-23 at 273 K and 298 K. Fit curves are obtained by the virial-type expression.

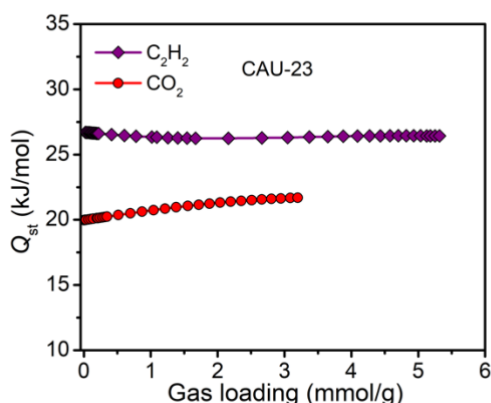


Figure S27. The heat of adsorption of CAU-23 for C₂H₂ and CO₂.

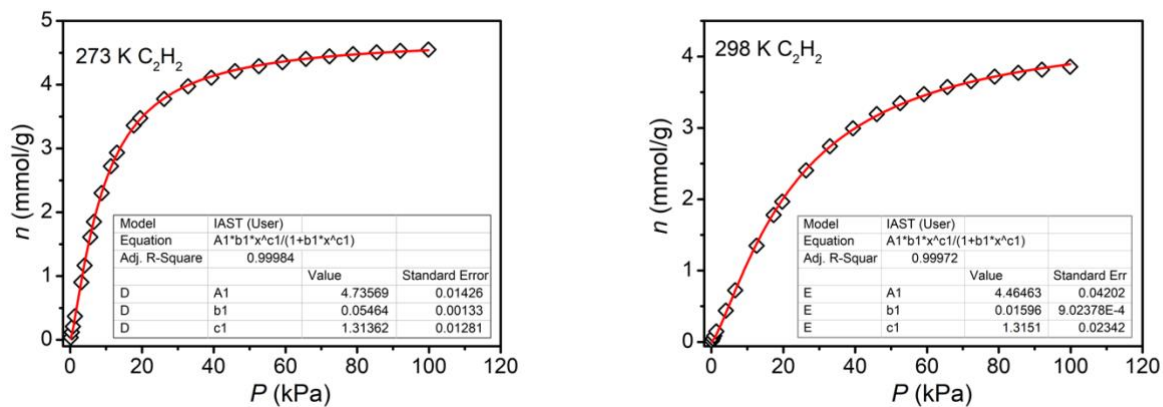


Figure S28. The graphs of the Single-site Langmuir-Freundlich equations fit for adsorption of C_2H_2 on CAU-10H at 273 K and 298 K.

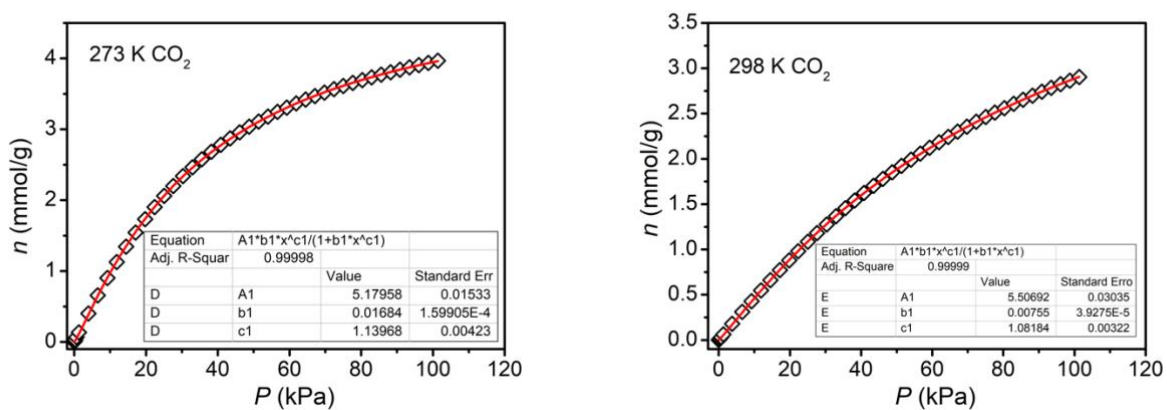


Figure S29. The graphs of the Single-site Langmuir-Freundlich equations fit for adsorption of CO_2 on CAU-10H at 273 K and 298 K.

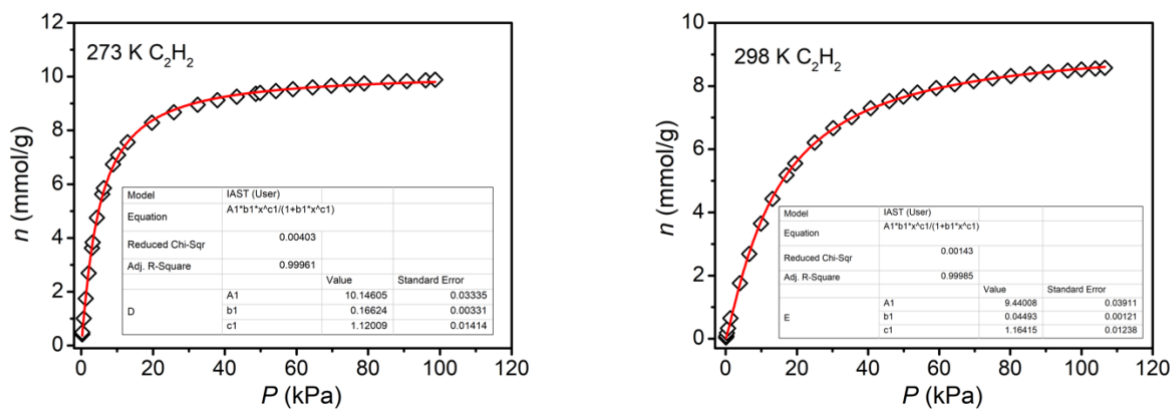


Figure S30. The graphs of the Single-site Langmuir-Freundlich equations fit for adsorption of C₂H₂ on MIL-160 at 273 K and 298 K.

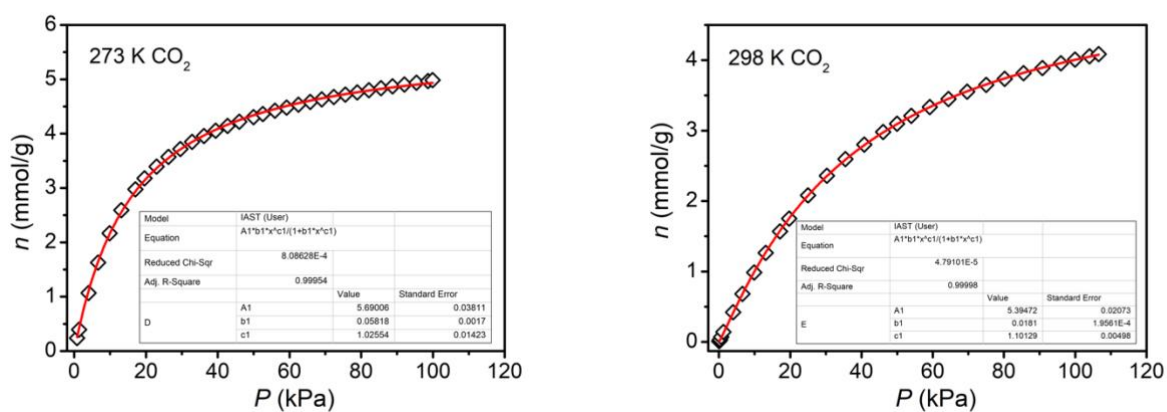


Figure S31. The graphs of the Single-site Langmuir-Freundlich equations fit for adsorption of CO₂ on MIL-160 at 273 K and 298 K.

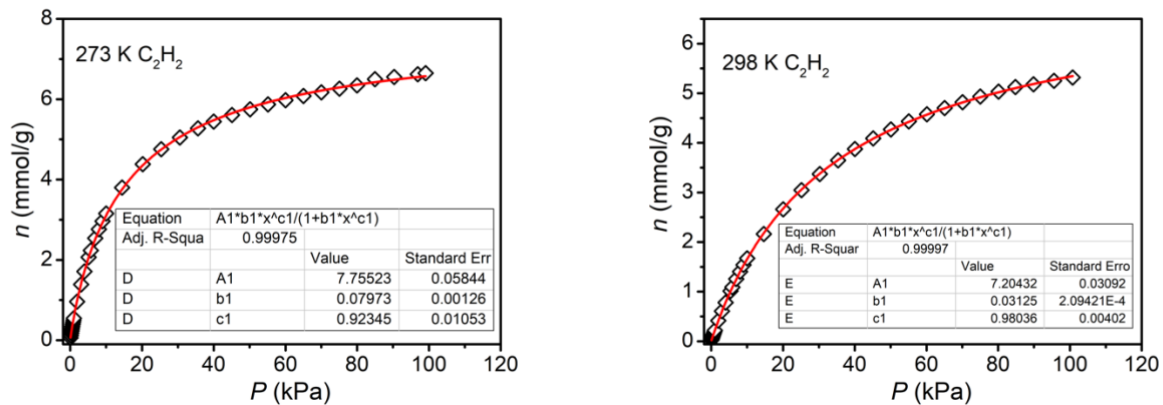


Figure S32. The graphs of the Single-site Langmuir-Freundlich equations fit for adsorption of C₂H₂ on CAU-23 at 273 K and 298 K.

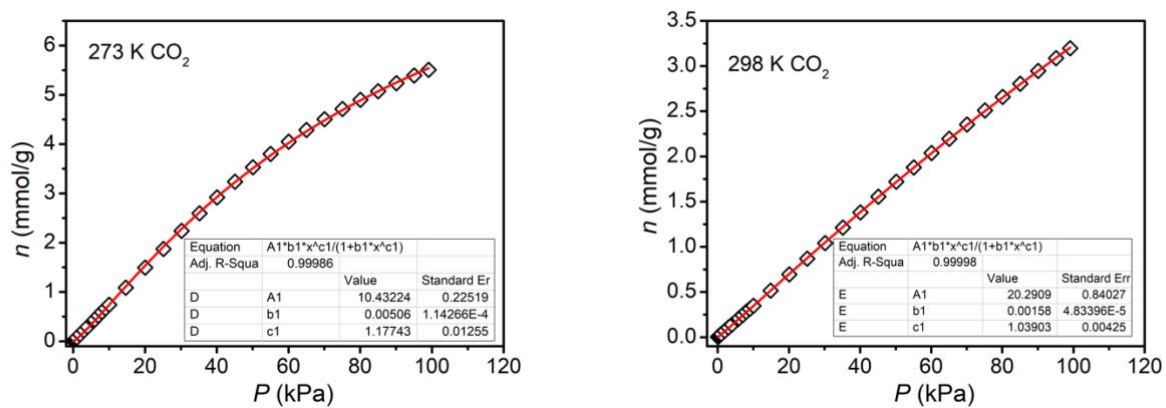


Figure S33. The graphs of the Single-site Langmuir-Freundlich equations fit for adsorption of CO₂ on CAU-23 at 273 K and 298 K.

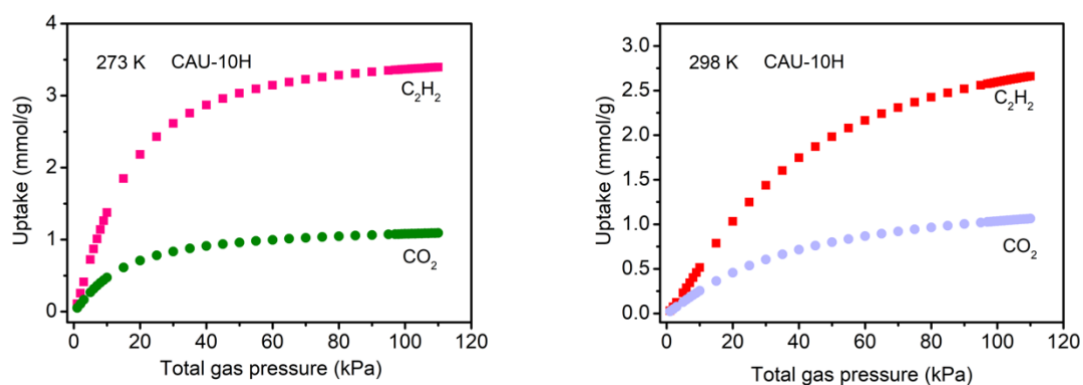


Figure S34. Mixture adsorption isotherms of CAU-10H for C_2H_2/CO_2 (50/50) at 273 K and 298 K as predicted by IAST.

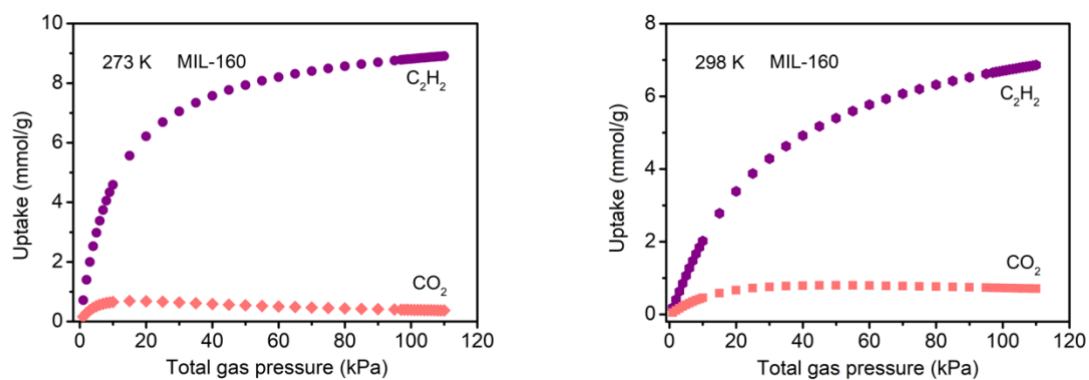


Figure S35. Mixture adsorption isotherms of MIL-160 for C_2H_2/CO_2 (50/50) at 273 K and 298 K as predicted by IAST.

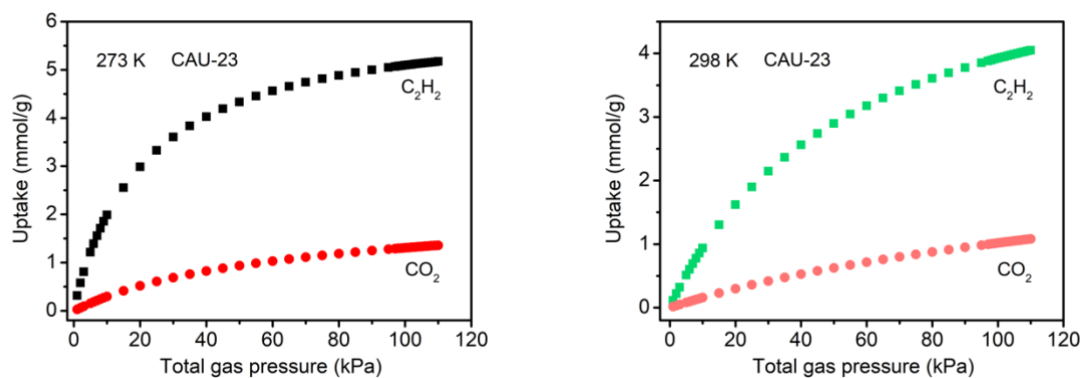


Figure S36. Mixture adsorption isotherms of CAU-23 for C_2H_2/CO_2 (50/50) at 273 K and 298 K as predicted by IAST.

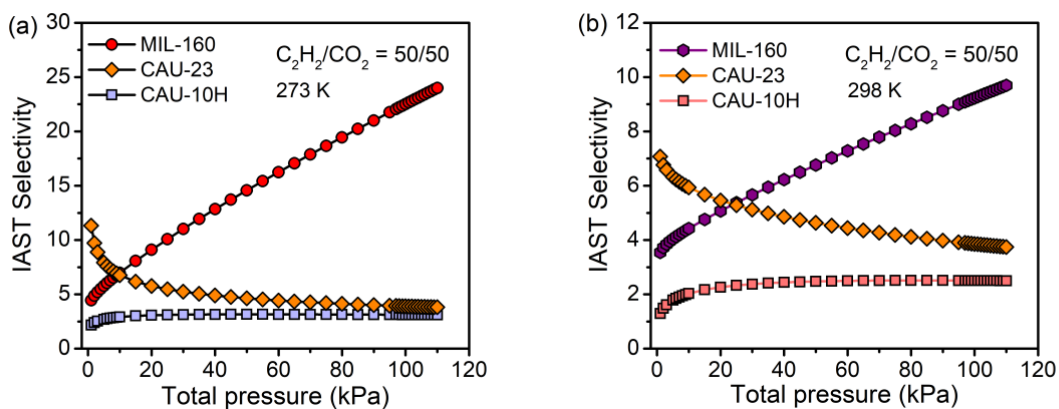


Figure S37. (a-b) Comparison of the IAST selectivity of these three MOFs for equimolar C_2H_2/CO_2 mixtures at 273 K and 298 K.

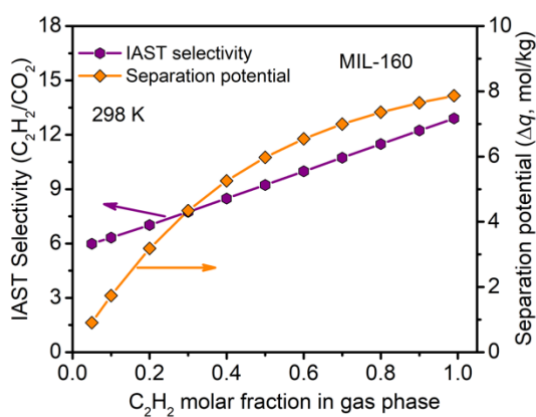


Figure S38. IAST selectivity and separation potential of C_2H_2/CO_2 mixtures with different C_2H_2 mole fractions at 100 kPa and 298 K.

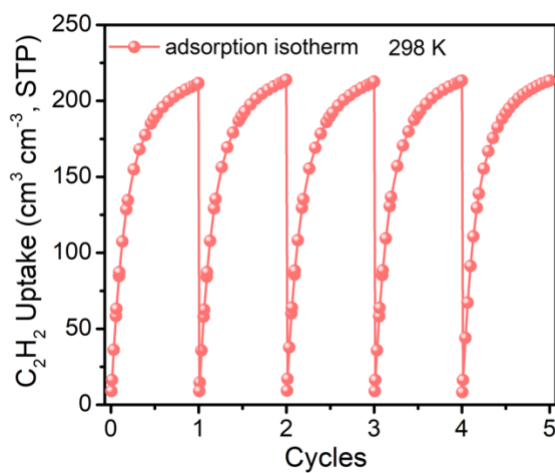


Figure S39. Cycles of C_2H_2 adsorption-desorption for MIL-160 at 298 K.

Breakthrough simulations

The performance of industrial fixed bed adsorbers is dictated by a combination of adsorption selectivity and uptake capacity. Transient breakthrough simulations were carried out for binary 50/50 or 90/10 C₂H₂/CO₂ mixtures in MIL-160, CAU-10H, CAU-23, FJU-90, FeNi-M' MOF, UTSA-74, ZJU-74, BSF-3, TIFSIX-2-Cu-i, JCM-1, MUF-17, and DICRO-4-Cu-i, operating at a total pressure of 100 kPa and 298 K, using the methodology described in the earlier publications.⁷⁻¹⁰ For the breakthrough simulations, the following parameter values were used: length of packed bed, $L = 0.3$ m; voidage of packed bed, $\varepsilon = 0.4$; superficial gas velocity at inlet, $u = 0.04$ m/s. The x -axis is the dimensionless time, $\tau = t \times u / (L \times \varepsilon)$, defined by dividing the actual time, t , by the characteristic time, $L\varepsilon/u$.

During the initial transience, the effluent gas contains pure CO₂ and this continues until C₂H₂ starts breaking through because its uptake capacity in the MOF has been reached. As in previous works,⁸ we define the breakthrough time for C₂H₂ τ_{break} as the time at which the C₂H₂ concentration in the outlet gas mixture is $< 0.05\%$. The gravimetric C₂H₂ capture capacity during the time interval 0 to τ_{break} , expressed in mols per kg adsorbent, is determined from a material balance. The breakthrough simulations demonstrate the potential of separating C₂H₂ from CO₂ during a certain time interval $\Delta\tau$.

Separation potential calculation

The separation performance in fixed bed adsorbers is dictated not only by selectivity, but also the uptake capacity. For this reason, a combined metric, called the separation potential (Δq), was introduced recently by Krishna.^{7, 10} This combined metric Δq , represents the difference of moles of component 1 (the more strongly adsorbed species) and component 2 (the less strongly adsorbed species) adsorbed in the per kg of adsorbent in the fixed bed.

$$\Delta q = q_1 - q_2 \frac{y_1}{y_2} \quad (5)$$

where q_1, q_2 are the molar loading (units: mol/kg) for mixture adsorption, calculated from the IAST or breakthrough simulation. The values of Δq_{IAST} were determined from IAST calculation. The values of Δq_{break} were determined from a rigorous material balance performed for each of the breakthrough simulations to determine the component uptakes.

Table S2. Summarized $\Delta\tau$, Δq_{IAST} , Δq_{break} and q_{break} values of representative porous materials for separation of binary 50/50 C₂H₂/CO₂ mixtures.

Materials	$\Delta\tau$	Separation potential based on IAST calculation (Δq_{IAST} , mol/kg)	Separation potential in the fixed bed (Δq_{break} , mol/kg)	C ₂ H ₂ adsorbed during 0- τ_{break} (q_{break} , mol/kg)	ref
MIL-160	304	6.00	5.02	5.82	This work
CAU-10H	77	1.56	1.40	2.16	This work
CAU-23	178	2.90	2.49	3.35	This work
UTSA-74a	214	3.41	2.99	3.47	11
FJU-90a	170	4.50	3.75	5.10	8
FeNi-M'MOF	207	3.76	3.32	3.51	12
ZJU-74	151	3.06	2.70	2.94	13
BSF-3	113	2.78	2.44	2.64	14
TIFSIX-2-Cu-i	100	2.58	2.18	3.35	14
JCM-1	145	2.43	2.12	2.87	14
MUF-17	134	2.10	1.79	3.64	14
DICRO-4-Cu-i	76	1.43	1.26	1.49	14

For comparing the performance of MIL-160 and other representative MOFs, the Δq_{IAST} and Δq_{break} were all calculated for them. It is noteworthy that for all MOFs, the Δq_{break} in the fixed bed adsorber is lower than the corresponding Δq_{IAST} value because of the distended nature of the breakthroughs in the fixed bed.

The $\Delta\tau$, Δq_{IAST} and Δq_{break} were summarized above, which also indicate that MIL-160 has the best separation ability. Generally speaking, the larger the capacity difference (Δq_{break}), the better separation performance the material has.

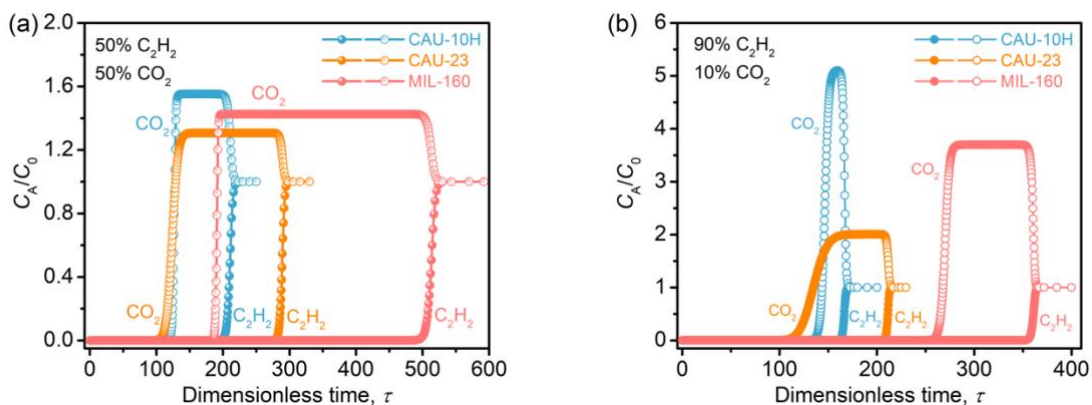


Figure S40. (a-b) Transient breakthrough simulations for the separation of C_2H_2/CO_2 (50/50 and 90/10, v/v) gas mixtures using MIL-160, CAU-10H, and CAU-23 at 298 K and 100 kPa.

As shown in **Figure S40**, the binary 50/50 or 90/10 C_2H_2/CO_2 mixtures can be effectively separated by these three MOFs. Notably, the retention time ($\Delta\tau$) and C_2H_2 productivity of MIL-160 is significantly higher than that of the other two MOFs under similar conditions (**Table S2**).

Column Breakthrough Experiments

The breakthrough experiments were carried out in a self-made dynamic mixed gas breakthrough set-up.⁸ A stainless steel column with inner dimensions of $\phi 4 \times 150$ mm was used for sample packing. Microcrystalline sample with particle size of 220-320 μm obtained via sieving was then packed into the column. The mixed gas flow and pressure were controlled by using a pressure controller valve and a mass flow controller. Outlet effluent from the column was continuously monitored using gas chromatography (GC-2014, SHIMADZU) with a thermal conductivity detector (TCD). The column packed with activated sample was firstly purged with He flow (50 mL min^{-1}) for 1 h at room temperature. The mixed gas flow rate during breakthrough process is 2 mL min^{-1} using 50/50 (v/v) $\text{C}_2\text{H}_2/\text{CO}_2$ at room temperature (298 K). After the breakthrough experiment, the sample was regenerated by purging the He gas flow (50 mL min^{-1}) for 2 h at room temperature.

Based on the mass balance, the gas adsorption capacities can be determined as follows:

$$q_i = \frac{C_i V}{22.4 \times m} \times \int_0^t \left(1 - \frac{F}{F_0}\right) dt \quad (6)$$

Where q_i is the equilibrium adsorption capacity of gas i (mmol g^{-1}), C_i is the feed gas concentration, V is the volumetric feed flow rate (mL min^{-1}), t is the adsorption time (min), F_0 and F are the inlet and outlet gas molar flow rates, respectively, and m is the mass of the adsorbent (g).

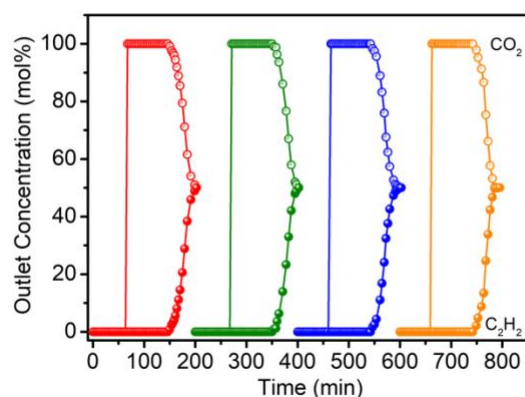


Figure S41. Experimental breakthrough curves for a cycling test of the equimolar C_2H_2/CO_2 mixture in a packed column with MIL-160 at 298 K and 1 bar.

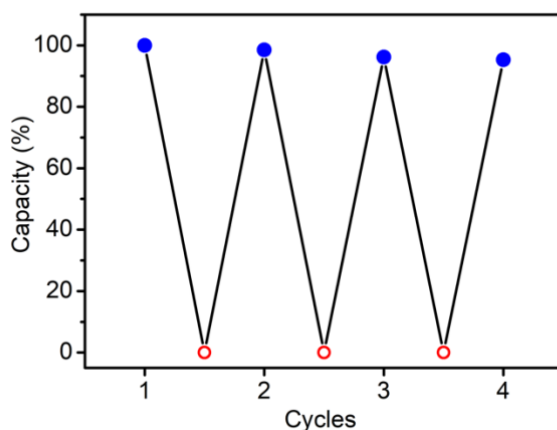


Figure S42. Cycling data of MIL-160 for successive C_2H_2 adsorption and desorption. Adsorption capacities are expressed in terms of percentage of uptake relative to the first cycle. Adsorption (blue circles) was collected at 298 K and 1 bar. Desorption (red circles) occurred by applying a helium gas flow (50 standard cubic centimeters per minute) for about 2 hours at 298 K.

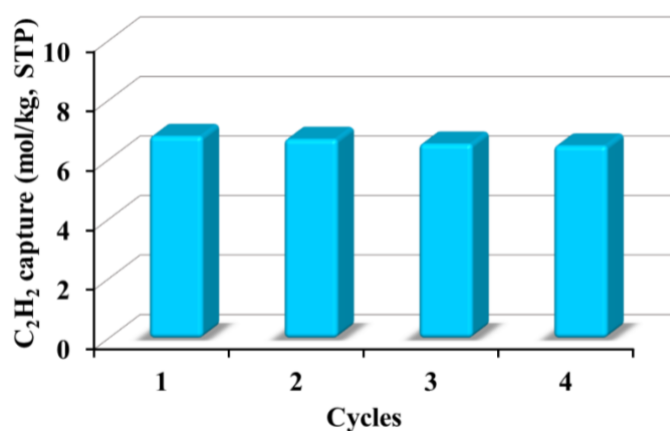


Figure S43. The values of C_2H_2 adsorption capacity of MIL-160 in multiple breakthrough experiments.

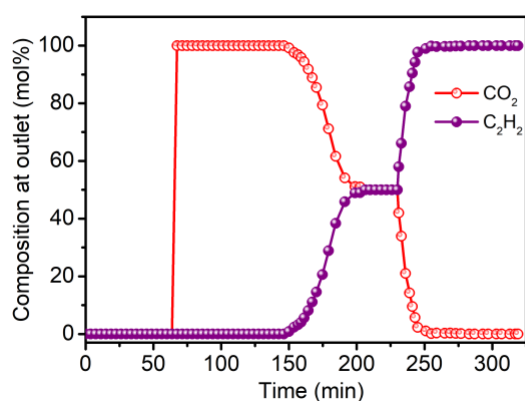


Figure S44. Experimental breakthrough curves for the adsorption of equimolar C_2H_2/CO_2 mixtures flowing through a fixed-bed of MIL-160 at 298 K with a total gas flow of 2 mL/minute at atmospheric pressure. After breakthrough of the C_2H_2 and reach up to an equimolar mixture composition, a helium purge was applied, leading to desorption of the C_2H_2 .

Table S3. Comparison of C_2H_2/CO_2 separation performances for some representative MOFs under ambient condition.

Materials	C_2H_2 uptake (cm^3/g)		CO_2 uptake (cm^3/g)	IAST selectivity (C_2H_2/CO_2)	C_2H_2 Capture (mol/kg)	T (K)	Q_{st} (kJ/mol)		Ref
	0.5 bar	1.0 bar					C_2H_2	CO_2	
MIL-160	172	191	90	10	6.8	298	31.8	26.9	This work
SIFSIX-Cu-TPA	168	185	107	5.3	6.25	298	39.1	25.7	15
SNNU-45	114.1	134	97.4	4.5	5.67	298	40	27.1	16
ZJU-280a	95	106	71	18.1	4.1	296	50.6	38.8	17
FeNi-M'MOF	91	96	61	24	2.96	298	27	24.5	12
ZJU-74a	76.7	85.7	66.3	36.5	3.64	296	45	30	13
BSF-3	69.6	80.4	47.3	16.3	2.9	298	42.7	22.4	14
ZJUT-2a	72	76	49	8.5	2.3	296	41.5	35.5	18
JCM-1	63.5	75	38	13.7	2.2	298	36.7	33.3	19
JNU-1	60.5	64	50.5	3.6	2.92	298	13	24	20
$Cu^I@UiO-66-(COOH)_2$	43	52	20	185	2.89	298	74.5	28.9	5

In situ Infrared (IR) spectroscopy: *In-situ* IR measurements were performed on a Nicolet 6700 FT-IR spectrometer using a liquid N₂-cooled mercury cadmium telluride (MCT-A) detector. The spectrometer is equipped with a vacuum cell that is placed in the main compartment with the sample at the focal point of the infrared beam. The samples (~5 mg) were gently pressed onto KBr pellet and placed into a cell that is connected to a vacuum line for evacuation. The samples were activated by overnight evacuation at 150 °C, and then cooled back to room temperature for C₂H₂ gas adsorption measurement.

Theoretical method for frequency calculation: MIL-160 linker was separated from the MOF and terminated using H atoms. *ab-initio* calculations were performed to optimize the structure of the linker. Vibrational frequency for the MIL-160 linker was calculated in VASP, using density functional theory (DFT). The finite difference method was used, where each ion was displaced by 0.1 Å along the coordinates and symmetry was utilized to calculate the Hessian matrix and obtain the vibrational frequencies by diagonalizing the resulting matrix.

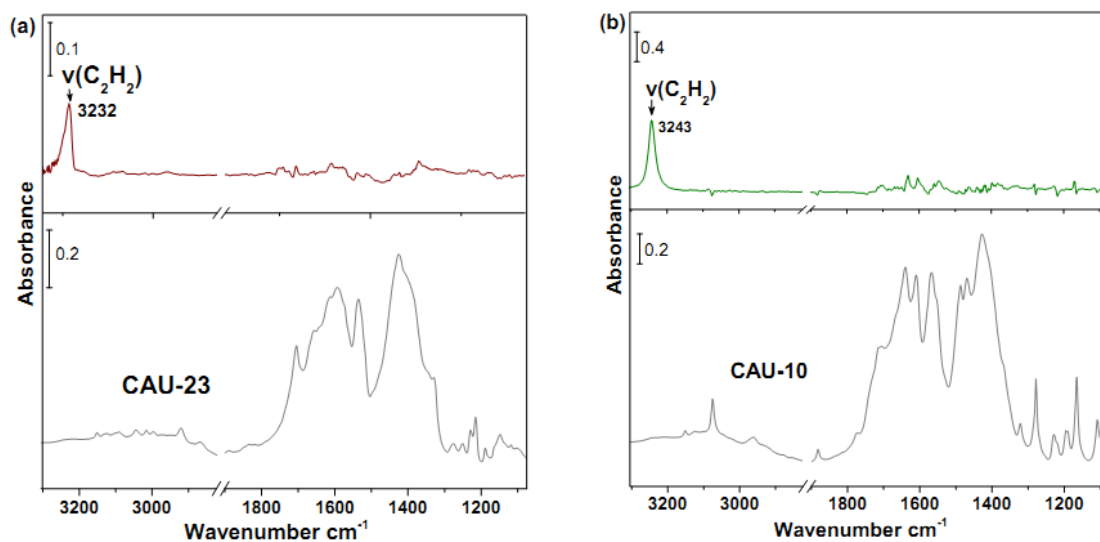


Figure S45. Full IR difference spectra showing the stretching band of adsorbed C₂H₂ inside CAU-23 (brown line in **a**) and CAU-10H (green line in **b**) upon loading C₂H₂ gas at ~400 Torr, referenced to the activated CAU-23 and CAU-10H, respectively, as represented in the bottom grey spectra. The signal of gas phase C₂H₂ is subtracted.

Table S4. Summary of selected MIL-160 vibrational modes associated with FDC linker.

Assignment	Position	
	<i>Exp.</i>	<i>Cal.</i>
Summation band	1743	
$\nu_{\text{as}}(\text{COO})$	1602-1580	
$\nu(\text{CC})$ of furan ring	1514	1529
$\nu_{\text{s}}(\text{COC}) + \nu(\text{CC})_{\text{furan ring}}$	1242	1264
$\nu_{\text{as}}(\text{COC}) + \delta(\text{CH})_{\text{ip}}$	1224	1214
$\nu_{\text{s}}(\text{COC})$ of furan ring	1178	1193
$\nu_{\text{as}}(\text{COC})$ of furan ring	1133	1149

Modeling Studies

The binding sites for C₂H₂ and CO₂ in MIL-160 were determined through classical molecular simulations. The single X-ray crystallographic structure that was published in reference²¹ for the material was used as a starting point to perform the parametrizations and simulations. All H atoms that were originally absent in the crystal structure were manually inserted where appropriate (i.e., on the 2,5-furandicarboxylate linkers and bridging hydroxide groups). The resultant structures were subject to geometry optimization, which was implemented with the CP2K program²² with the crystallographically determined basis vectors held constant.

All atoms of the optimized structure of MIL-160 were treated with Lennard-Jones (LJ) parameters (ϵ and σ),²³ point partial charges, and point polarizabilities in order to model repulsion/dispersion, stationary electrostatic, and many-body polarization interactions, respectively. The LJ parameters for all atoms were taken from the Universal Force Field (UFF).²⁴ The partial charges for the unique atoms in MIL-160 were determined through the extended charge equilibration (EQ_{eq}) method.²⁵ The exponential damping-type polarizability values for all C, H, and O atoms were taken from a carefully parametrized set provided by the work of van Duijnen and Swart.²⁶ The polarizability parameter for Al³⁺ was determined by fitting a molecular polarizability tensor to one that was obtained from quantum mechanical calculations for a fragment containing this ion using the method described in previous work.²⁷ The optimal polarizability value for Al³⁺ was calculated to be 2.3980 Å³.

Simulated annealing (SA) calculations²⁸ were performed for a single molecule of each adsorbate through a canonical Monte Carlo (NVT) process in a 1 × 1 × 2 supercell of MIL-160. All MOF atoms were kept fixed at their crystallographic positions throughout the simulations. A spherical cut-off distance of 10.48995 Å, representing half the shortest supercell dimension length, was used for the simulations. C₂H₂ and CO₂ were modeled using polarizable potentials of the respective adsorbates that were developed previously.²⁹⁻³⁰ The total potential energy of the MOF–adsorbate system was calculated through the sum of the repulsion/dispersion, stationary electrostatic, and many-body polarization energies. These were calculated using the LJ potential,²² the Ewald summation technique,³¹⁻³² and a Thole-Applequist type model,³³⁻³⁶ respectively. SA calculations for each adsorbate utilized an initial temperature of 500 K, and this temperature was scaled by a factor

of 0.99999 after every 10^3 Monte Carlo (MC) steps. The simulations continued until 10^6 MC steps were reached; at this point, the temperature of the system is below 10 K and the adsorbate is already localized in its energy minimum position in the MOF. All simulations were carried out using the Massively Parallel Monte Carlo (MPMC) code.³⁷⁻³⁸

Next, canonical Monte Carlo (CMC) simulations was performed for a single molecule of C_2H_2 and CO_2 , individually, positioned at their global minimum in MIL-160. This was done in order to evaluate the averaged classical potential energy for all three adsorbates about their energy minimum position in the material. The CMC simulations were performed at a temperature of 20 K and a pressure of 1.0 atm. These simulations ran for a total of 10^6 MC steps to ensure reasonable ensemble averages for the total potential energy of the system. The averaged classical potential energies for C_2H_2 , and CO_2 localized about their energy minimum position in MIL-160 are presented in **Table S5**.

Table S5. Calculated averaged total potential energies (in kJ mol^{-1}) for a single C_2H_2 , and CO_2 molecule, individually, positioned at their global minimum in MIL-160 as determined from CMC simulations at 20 K/1.0 atm.

MOFs	Adsorbate	MOF–Adsorbate Energy (kJ mol^{-1})	
MIL-160	C_2H_2	site I	–37.8
		site II	–35.0
		site III	–35.6
	CO_2	site I	–32.7
		site II	–29.7

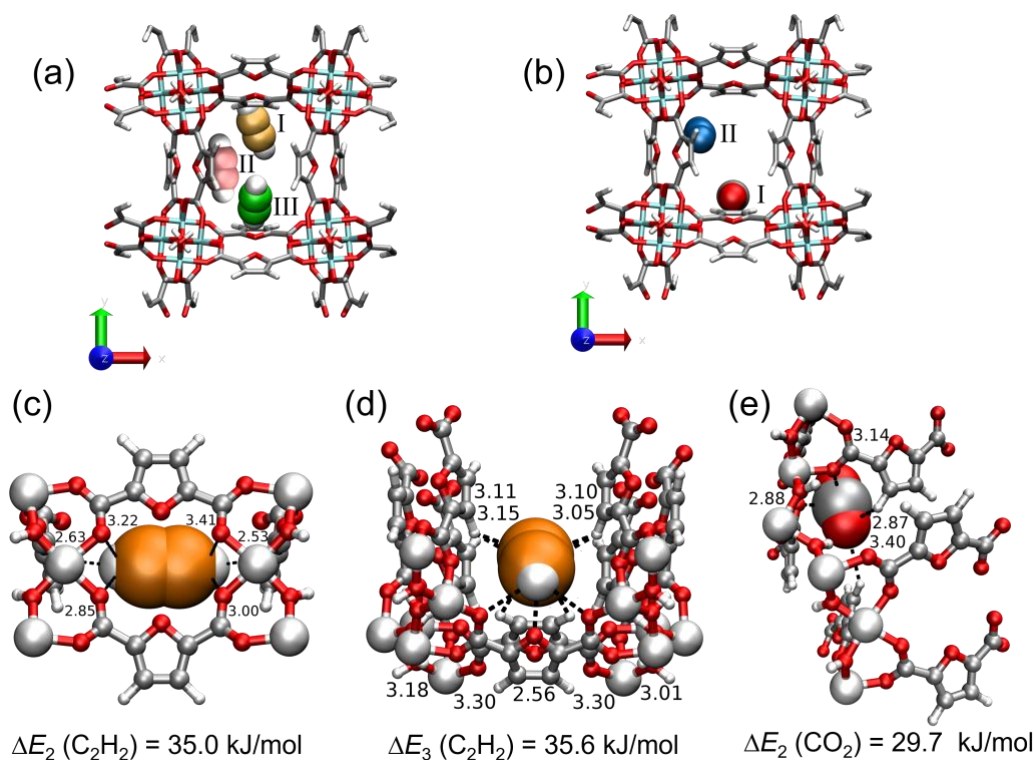


Figure S46. The canonical Monte Carlo (CMC) calculated adsorption configurations of (a) C_2H_2 (orange = primary site, pink = secondary site, green = tertiary site) and (b) CO_2 in MIL-160 (blue = secondary site). (c) Simulated secondary binding site of C_2H_2 , (d) tertiary binding site of C_2H_2 , and (e) secondary binding site of CO_2 in MIL-160. (The distances unit is Å)

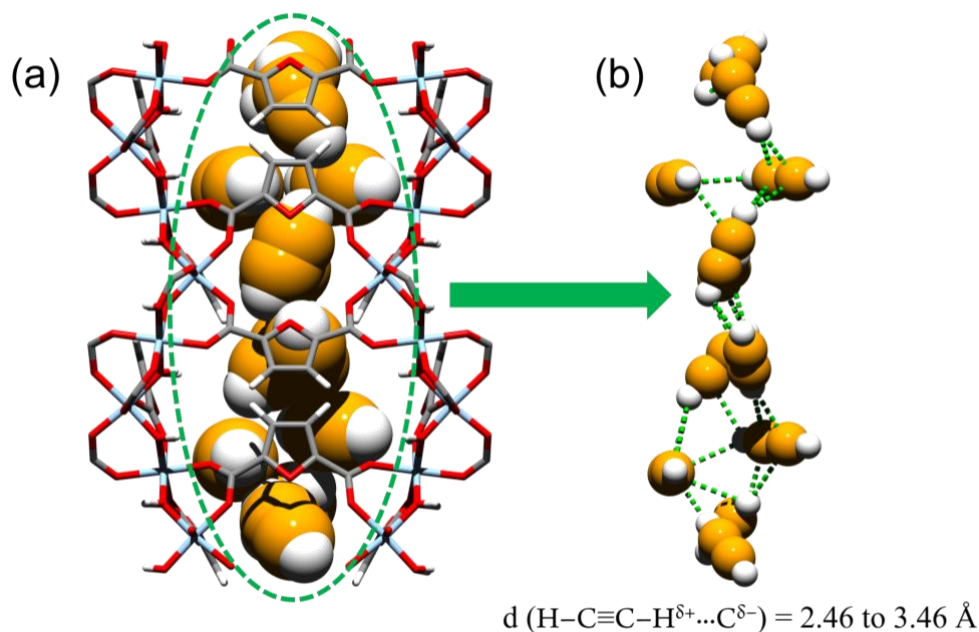


Figure S47. (a-b) Snapshot of canonical Monte Carlo runs of a saturated corridor loaded with C_2H_2 illustrating favorable adsorbate-adsorbate interactions.

An additional series of Simulated annealing (SA) calculations were performed on C₂H₂ and CO₂ in MIL-160 in the same manner described above, with the exception that a temperature scaling factor of 0.999 was applied, in order to locate local energy minima. For C₂H₂, secondary and tertiary sorption sites were found (**Figures S46a, c, and d**), while CO₂ exhibited only a secondary binding site (**Figures S46b and e**). The binding energies, obtained in the manner discussed above, were found to be between 2 ~ 3 kJ/mol less than those observed at the primary binding site (**Table S5**).

Further investigation of adsorption sites in MIL-160 was undertaken via examination of a simulation cell with a single saturated column. This system was subjected to CMC simulations at 273 K. In the case of C₂H₂, the three adsorption sites reported above were observed in the system. Of particular note is that all adsorption C₂H₂ molecules are all roughly perpendicular to the constricted MOF channels. This results in significant favorable adsorbate-adsorbate interaction as the molecules stack in brick-like layering with hydrogen atoms on one C₂H₂ coordinating to one or more carbon atoms on proximal neighbors (**Figure S47**). Approximating the Q_{st} of the system by taking the average intermolecular energy per adsorbate provides a value of 35.7 kJ/mol. A single particle run under the same conditions produced an average intermolecular energy of 31.5 kJ/mol showing that adsorbate-adsorbate interactions increase adsorption strength by 4.2 kJ/mol in a saturated corridor. These values are in reasonable agreement with Q_{st} derived from the experimental adsorption isotherms (**Figure S24**) and explain the derivation of the increasing trend of the graph.

***Ab initio* calculation method:** All results were obtained by *ab initio* calculations performed in VASP (Vienna Ab Initio Simulation Package) using density functional theory (DFT).³⁹⁻⁴⁰ The vdW-DF functional was used to take into account important van der Waals interactions.⁴¹⁻⁴² The MOF unit cells were optimized until the force acting between atoms is below 5 meV/Å, with SCF convergence of 0.1 meV and the plane-wave energy cut-off set at 600 eV. The diffusion of guest molecules through the MOFs was studied by determining the transition state energies using the climbing nudged elastic band (cNEB) method.⁴³⁻⁴⁴ The vibrational frequency calculation was started by separating the linker from the MOF and terminated using H atoms. *Ab initio* calculations were performed to optimize the structure of the linker. Vibrational frequencies for the linker were calculated using the finite difference method. Each ion was displaced by 0.1 Å along the coordinates and symmetry was utilized to calculate the Hessian matrix and obtain the vibrational frequencies by diagonalizing the resulting matrix.

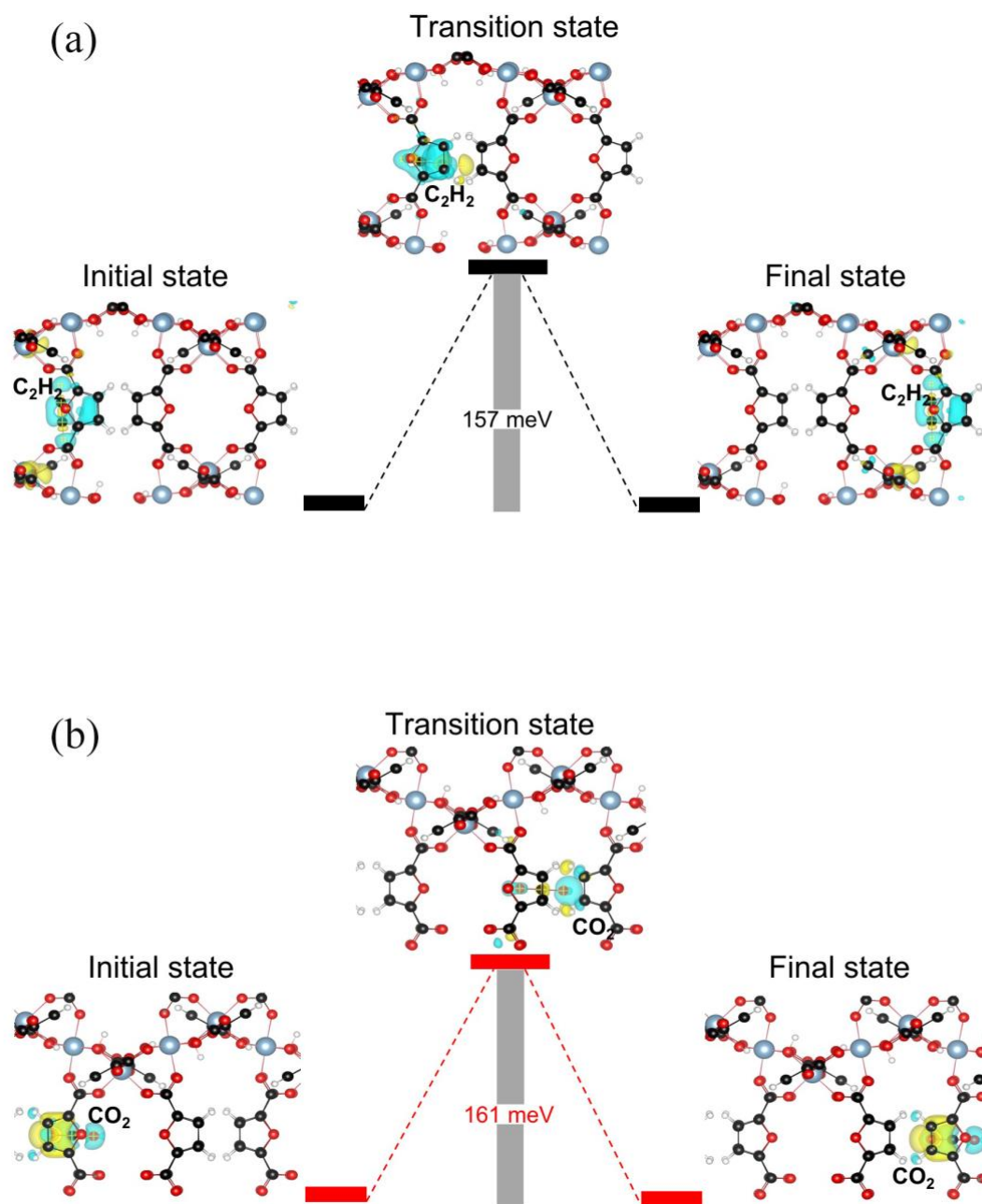


Figure S48. Induced charge densities at an iso-level of 0.0002 electrons/Å³ of initial, transition, and final state configurations for (a) C₂H₂ and (b) CO₂ diffusion along MIL-160. Yellow areas represent a charge accumulation and blue areas a depletion upon interaction with the molecules. The corresponding diffusion barrier energies of C₂H₂ and CO₂ are also provided.

Table S6. Comparison of C₂H₂ storage performances at ambient condition for some representative MOFs.

Materials	S_{BET} (m ² /g)	V_{p}^a (cm ³ /g)	ρ^b (g/cm ³)	C ₂ H ₂ uptake (1 bar)		T (K)	$Q_{\text{st},n=0}$ (kJ/mol)	OMS density ^c (mmol/g)	Storage density ^d (g/cm ³)	Ref
				(cm ³ /g)	(cm ³ /cm ³)					
CoMOF-74	1018	0.51	1.169	197	230	295	50.1	6.41	0.267	45
MIL-160	1138	0.428	1.117	191	213	298	31.8	0	0.247	This work
CAU-23	1320	0.528	1.074	119	128	298	26.7	0	0.148	This work
CAU-10H	680	0.294	1.159	86.4	100	298	26.2	0	0.116	This work
CPM-733-dps	1883	0.750	0.872	234	204	298	25.7	1.88	0.237	46
FJI-H8	2025	0.82	0.873	224	196	295	32.0	3.59	0.228	47
ZJU-12a	2316	0.938	0.799	239	191	298	29	3.13	0.222	48
HKUST-1	1781	0.70	0.881	201	177	295	34.0	4.96	0.205	49
NJU-Bai17	2423	0.914	0.787	222.4	176	296	38	4.03	0.204	50
SIFSIX-Cu-TPA	1330	0.52	0.924	185	171	298	39.1	0	0.198	15
MgMOF-74	927	0.607	0.909	184	167.2	296	34.0	8.24	0.194	45
SIFSIX-1-Cu	1178	0.57	0.864	190.4	164.5	298	30	0	0.191	51
ZJU-40a	2858	1.06	0.750	216	162	298	34.5	3.44	0.188	52
ZJNU-54	2134	0.871	0.761	211	160	295	35.4	3.66	0.186	53
MFM-188a	2568	1.12	0.666	232	155	295	32.5	3.3	0.180	54
NOTT-300	1370	0.433	1.062	142	150.8	293	32	0	0.175	55
FJU-90a	1572	0.65	0.816	180	147	298	25.1	0	0.171	8
ZJNU-47	2638	1.031	0.689	213	146.8	295	35.0	3.44	0.170	56
UTSA-74a	830	0.39	1.34	108	145.0	298	31.5	3.08	0.168	11
FJU-101a	1935	0.77	0.835	172.5	144	296	35.9	2.79	0.167	57
Cu-TDPAT	1938	0.93	0.782	178	139.2	298	30.8	3.74	0.162	58
MOF-505	1547	0.60	0.926	148	137	296	24.7	4.41	0.159	49
ZJNU-34(NH ₂)	2459	0.969	0.706	193.8	136.9	298	34.2	3.68	0.159	59
SNNU-27-Fe	1570	0.876	0.74	182.4	135	298	24.1	0	0.157	60

ZJU-5a	2823	1.074	0.679	193	131	298	35.8	3.87	0.152	61
PCN-16	2273	1.06	0.724	176	127.4	296	34.5	4.19	0.148	62
Cu ₆ (DDC) ₃	2410	0.98	0.757	164	124.1	298	33.5	3.37	0.144	63
Cu-EBTC	1852	1.000	0.772	160	123.5	295	34.5	4.19	0.143	64
NOTT-101	2755	1.058	0.657	184	121	298	32.8	3.44	0.140	62

^a V_p : pore volume ($\text{cm}^3 \text{g}^{-1}$)

^b ρ : crystal density (g cm^{-3})

^c OMS density: The OMS density of MOFs was calculated based on the crystal structure information files, OMS = open metal site.

^d Storage density: Density of adsorbed C_2H_2 in bulk material.

Supplementary References

- (1) Permyakova, A.; Skrylnyk, O.; Courbon, E.; Affram, M.; Wang, S.; Lee, U. H.; Valekar, A. H.; Nouar, F.; Mouchaham, G.; Devic, T.; De Weireld, G.; Chang, J.-S.; Steunou, N.; Frère, M.; Serre, C., Synthesis Optimization, Shaping, and Heat Reallocation Evaluation of the Hydrophilic Metal–Organic Framework MIL-160(Al). *ChemSusChem* **2017**, *10*, 1419-1426.
- (2) Leubner, S.; Stäglich, R.; Franke, J.; Jacobsen, J.; Gosch, J.; Siegel, R.; Reinsch, H.; Maurin, G.; Senker, J.; Yot, P. G.; Stock, N., Solvent Impact on the Properties of Benchmark Metal–Organic Frameworks: Acetonitrile-Based Synthesis of CAU-10, Ce-Uio-66, and Al-MIL-53. *Chem. Eur. J.* **2020**, *26*, 3877-3883.
- (3) Schlusener, C.; Jordan, D. N.; Xhinovci, M.; Matemb Ma Ntep, T. J.; Schmitz, A.; Giesen, B.; Janiak, C., Probing the limits of linker substitution in aluminum MOFs through water vapor sorption studies: mixed-MOFs instead of mixed-linker CAU-23 and MIL-160 materials. *Dalton Trans.* **2020**, *49*, 7373-7383.
- (4) Myers, A. L.; Prausnitz, J. M., Thermodynamics of Mixed-Gas Adsorption. *AIChE J.* **1965**, *11*, 121-127.
- (5) Zhang, L.; Jiang, K.; Yang, L.; Li, L.; Hu, E.; Yang, L.; Shao, K.; Xing, H.; Cui, Y.; Yang, Y.; Li, B.; Chen, B.; Qian, G., Benchmark C₂H₂/CO₂ Separation in an Ultra-Microporous Metal-Organic Framework via Copper(I)-Alkynyl Chemistry. *Angew. Chem. Int. Ed.* **2021**, *60*, 15995-16002.
- (6) Xie, Y.; Cui, H.; Wu, H.; Lin, R. B.; Zhou, W.; Chen, B., Electrostatically Driven Selective Adsorption of Carbon Dioxide over Acetylene in an Ultramicroporous Material. *Angew. Chem. Int. Ed.* **2021**, *60*, 9604-9609.
- (7) Krishna, R., Screening metal–organic frameworks for mixture separations in fixed-bed adsorbers using a combined selectivity/capacity metric. *RSC Adv.* **2017**, *7*, 35724-35737.
- (8) Ye, Y.; Ma, Z.; Lin, R.-B.; Krishna, R.; Zhou, W.; Lin, Q.; Zhang, Z.; Xiang, S.; Chen, B., Pore Space Partition within a Metal–Organic Framework for Highly Efficient C₂H₂/CO₂ Separation. *J. Am. Chem. Soc.* **2019**, *141*, 4130–4136.
- (9) Krishna, R., Methodologies for screening and selection of crystalline microporous materials in mixture separations. *Sep. Purif. Technol.* **2018**, *194*, 281-300.
- (10) Krishna, R., Metrics for Evaluation and Screening of Metal–Organic Frameworks for Applications in Mixture Separations. *ACS Omega* **2020**, *5*, 16987-17004.
- (11) Luo, F.; Yan, C.; Dang, L.; Krishna, R.; Zhou, W.; Wu, H.; Dong, X.; Han, Y.; Hu, T. L.; O'Keeffe, M.; Wang, L.; Luo, M.; Lin, R. B.; Chen, B., UTSA-74: A MOF-74 Isomer with Two Accessible Binding Sites per Metal Center for Highly Selective Gas Separation. *J. Am. Chem. Soc.* **2016**, *138*, 5678-5684.
- (12) Gao, J.; Qian, X.; Lin, R. B.; Krishna, R.; Wu, H.; Zhou, W.; Chen, B., Mixed Metal-Organic Framework with Multiple Binding Sites for Efficient C₂H₂/CO₂ Separation. *Angew. Chem. Int. Ed.* **2020**, *59*, 4396-4400.
- (13) Pei, J.; Shao, K.; Wang, J. X.; Wen, H. M.; Yang, Y.; Cui, Y.; Krishna, R.; Li, B.; Qian, G., A Chemically Stable Hofmann-Type Metal-Organic Framework with Sandwich-Like Binding Sites for Benchmark Acetylene Capture. *Adv. Mater.* **2020**, *32*, 1908275.
- (14) Zhang, Y.; Hu, J.; Krishna, R.; Wang, L.; Yang, L.; Cui, X.; Duttwyler, S.; Xing, H., Rational Design of Microporous MOFs with Anionic Boron Cluster Functionality and Cooperative Dihydrogen Binding Sites for Highly Selective Capture of Acetylene. *Angew. Chem. Int. Ed.* **2020**, *59*, 17664-17669.
- (15) Li, H.; Liu, C.; Chen, C.; Di, Z.; Yuan, D.; Pang, J.; Wei, W.; Wu, M.; Hong, M., An Unprecedented Pillar-Cage Fluorinated Hybrid Porous Framework with Highly Efficient Acetylene Storage and Separation. *Angew. Chem. Int. Ed.* **2021**, *60*, 7547-7552.
- (16) Li, Y. P.; Wang, Y.; Xue, Y. Y.; Li, H. P.; Zhai, Q. G.; Li, S. N.; Jiang, Y. C.; Hu, M. C.; Bu, X., Ultramicroporous Building Units as a Path to Bi-microporous Metal-Organic Frameworks with High Acetylene Storage and Separation Performance. *Angew. Chem. Int. Ed.* **2019**, *58*, 13590-13595.
- (17) Qian, Q.-L.; Gu, X.-W.; Pei, J.; Wen, H.-M.; Wu, H.; Zhou, W.; Li, B.; Qian, G., A novel anion-pillared metal–organic

- framework for highly efficient separation of acetylene from ethylene and carbon dioxide. *J. Mater. Chem. A* **2021**, *9*, 9248-9255.
- (18) Wen, H. M.; Liao, C.; Li, L.; Yang, L.; Wang, J.; Huang, L.; Li, B.; Chen, B.; Hu, J., Reversing C₂H₂-CO₂ adsorption selectivity in an ultramicroporous metal-organic framework platform. *Chem. Commun.* **2019**, *55*, 11354-11357.
- (19) Lee, J.; Chuah, C. Y.; Kim, J.; Kim, Y.; Ko, N.; Seo, Y.; Kim, K.; Bae, T. H.; Lee, E., Separation of Acetylene from Carbon Dioxide and Ethylene by a Water-Stable Microporous Metal-Organic Framework with Aligned Imidazolium Groups inside the Channels. *Angew. Chem. Int. Ed.* **2018**, *57*, 7869-7873.
- (20) Zeng, H.; Xie, M.; Huang, Y. L.; Zhao, Y.; Xie, X. J.; Bai, J. P.; Wan, M. Y.; Krishna, R.; Lu, W.; Li, D., Induced Fit of C₂H₂ in a Flexible MOF Through Cooperative Action of Open Metal Sites. *Angew. Chem. Int. Ed.* **2019**, *58*, 8515-8519.
- (21) Wahiduzzaman, M.; Lenzen, D.; Maurin, G.; Stock, N.; Wharmby, M. T., Rietveld Refinement of MIL-160 and Its Structural Flexibility Upon H₂O and N₂ Adsorption. *Eur. J. Inorg. Chem.* **2018**, *2018*, 3626-3632.
- (22) Kuhne, T. D.; Iannuzzi, M.; Del Ben, M.; Rybkin, V. V.; Seewald, P.; Stein, F.; Laino, T.; Khaliullin, R. Z.; Schutt, O.; Schifmann, F.; Golze, D.; Wilhelm, J.; Chulkov, S.; Bani-Hashemian, M. H.; Weber, V.; Borstnik, U.; Taillefumier, M.; Jakobovits, A. S.; Lazzaro, A.; Pabst, H.; Muller, T.; Schade, R.; Guidon, M.; Andermatt, S.; Holmberg, N.; Schenter, G. K.; Hehn, A.; Bussy, A.; Belleflamme, F.; Tabacchi, G.; Gloss, A.; Lass, M.; Bethune, I.; Mundy, C. J.; Plessl, C.; Watkins, M.; VandeVondele, J.; Krack, M.; Hutter, J., CP2K: An electronic structure and molecular dynamics software package - Quickstep: Efficient and accurate electronic structure calculations. *J. Chem. Phys.* **2020**, *152*, 194103.
- (23) Jones, J. E., On the determination of molecular fields. —II. From the equation of state of a gas. *Proc. R. Soc. A* **1924**, *106*, 463-477.
- (24) Rappe, A. K.; Casewit, C. J.; Colwell, K. S.; Goddard, W. A.; Skiff, W. M., UFF, a full periodic table force field for molecular mechanics and molecular dynamics simulations. *J. Am. Chem. Soc.* **1992**, *114*, 10024-10035.
- (25) Wilmer, C. E.; Kim, K. C.; Snurr, R. Q., An Extended Charge Equilibration Method. *J. Phys. Chem. Lett.* **2012**, *3*, 2506-2511.
- (26) van Duijnen, P. T.; Swart, M., Molecular and Atomic Polarizabilities: Thole's Model Revisited. *J. Phys. Chem. A* **1998**, *102*, 2399-2407.
- (27) Forrest, K. A.; Pham, T.; Georgiev, P. A.; Embs, J. P.; Waggoner, N. W.; Hogan, A.; Humphrey, S. M.; Eckert, J.; Space, B., Inelastic Neutron Scattering and Theoretical Studies of H₂ Sorption in a Dy(III)-Based Phosphine Coordination Material. *Chem. Mater.* **2015**, *27*, 7619-7626.
- (28) Kirkpatrick, S.; Gelatt, C. D.; Vecchi, M. P., Optimization by Simulated Annealing. *Science* **1983**, *220*, 671.
- (29) Franz, D. M.; Dyott, Z. E.; Forrest, K. A.; Hogan, A.; Pham, T.; Space, B., Simulations of hydrogen, carbon dioxide, and small hydrocarbon sorption in a nitrogen-rich rht-metal-organic framework. *Phys. Chem. Chem. Phys.* **2018**, *20*, 1761-1777.
- (30) Mullen, A. L.; Pham, T.; Forrest, K. A.; Cioce, C. R.; McLaughlin, K.; Space, B., A Polarizable and Transferable PHAST CO₂ Potential for Materials Simulation. *J. Chem. Theory Comput.* **2013**, *9*, 5421-5429.
- (31) Ewald, P. P., Die Berechnung optischer und elektrostatischer Gitterpotentiale. *Ann. Phys.* **1921**, *369*, 253-287.
- (32) Wells, B. A.; Chaffee, A. L., Ewald Summation for Molecular Simulations. *J. Chem. Theory Comput.* **2015**, *11*, 3684-3695.
- (33) Applequist, J.; Carl, J. R.; Fung, K.-K., Atom dipole interaction model for molecular polarizability. Application to polyatomic molecules and determination of atom polarizabilities. *J. Am. Chem. Soc.* **1972**, *94*, 2952-2960.
- (34) Thole, B. T., Molecular polarizabilities calculated with a modified dipole interaction. *Chem. Phys.* **1981**, *59*, 341-350.
- (35) McLaughlin, K.; Cioce, C. R.; Pham, T.; Belof, J. L.; Space, B., Efficient calculation of many-body induced electrostatics in molecular systems. *J. Chem. Phys.* **2013**, *139*, 184112.
- (36) Bode, K. A.; Applequist, J., A New Optimization of Atom Polarizabilities in Halomethanes, Aldehydes, Ketones, and

- Amides by Way of the Atom Dipole Interaction Model. *J. Phys. Chem.* **1996**, *100*, 17820-17824.
- (37) Belof, J. L.; Space, B., Massively Parallel Monte Carlo (MPMC). Available on GitHub. <https://github.com/mpmccode/mpmc>. **2012**.
- (38) Franz, D. M.; Belof, J. L.; McLaughlin, K.; Cioce, C. R.; Tudor, B.; Hogan, A.; Laratelli, L.; Mulcair, M.; Mostrom, M.; Navas, A.; Stern, A. C.; Forrest, K. A.; Pham, T.; Space, B., MPMC and MCMD: Free High-Performance Simulation Software for Atomistic Systems. *Adv. Theory Simul.* **2019**, *2*, 1900113.
- (39) Kresse, G.; Furthmüller, J., Efficient iterative schemes for ab initio total-energy calculations using a plane-wave basis set. *Physical Review B* **1996**, *54*, 11169-11186.
- (40) Kresse, G.; Joubert, D., From ultrasoft pseudopotentials to the projector augmented-wave method. *Physical Review B* **1999**, *59*, 1758-1775.
- (41) Thonhauser, T.; Cooper, V. R.; Li, S.; Puzder, A.; Hyldgaard, P.; Langreth, D. C., Van der Waals density functional: Self-consistent potential and the nature of the van der Waals bond. *Physical Review B* **2007**, *76*, 125112.
- (42) Langreth, D. C.; Lundqvist, B. I.; Chakarova-Käck, S. D.; Cooper, V. R.; Dion, M.; Hyldgaard, P.; Kelkkanen, A.; Kleis, J.; Kong, L.; Li, S.; Moses, P. G.; Murray, E.; Puzder, A.; Rydberg, H.; Schröder, E.; Thonhauser, T., A density functional for sparse matter. *Journal of Physics: Condensed Matter* **2009**, *21*, 084203.
- (43) Henkelman, G.; Jónsson, H., Improved tangent estimate in the nudged elastic band method for finding minimum energy paths and saddle points. *J. Chem. Phys.* **2000**, *113*, 9978-9985.
- (44) Henkelman, G.; Uberuaga, B. P.; Jónsson, H., A climbing image nudged elastic band method for finding saddle points and minimum energy paths. *J. Chem. Phys.* **2000**, *113*, 9901-9904.
- (45) Xiang, S.; Zhou, W.; Zhang, Z.; Green, M. A.; Liu, Y.; Chen, B., Open metal sites within isostructural metal-organic frameworks for differential recognition of acetylene and extraordinarily high acetylene storage capacity at room temperature. *Angew. Chem. Int. Ed.* **2010**, *49*, 4615-4618.
- (46) Wang, Y.; Jia, X.; Yang, H.; Wang, Y.; Chen, X.; Hong, A. N.; Li, J.; Bu, X.; Feng, P., A Strategy for Constructing Pore-Space-Partitioned MOFs with High Uptake Capacity for C₂ Hydrocarbons and CO₂. *Angew. Chem. Int. Ed.* **2020**, *59*, 19027-19030.
- (47) Pang, J.; Jiang, F.; Wu, M.; Liu, C.; Su, K.; Lu, W.; Yuan, D.; Hong, M., A porous metal-organic framework with ultrahigh acetylene uptake capacity under ambient conditions. *Nat. Commun.* **2015**, *6*, 7575.
- (48) Duan, X.; Cui, Y.; Yang, Y.; Qian, G., A novel methoxy-decorated metal-organic framework exhibiting high acetylene and carbon dioxide storage capacities. *CrystEngComm* **2017**, *19*, 1464-1469.
- (49) Xiang, S.; Zhou, W.; Gallegos, J. M.; Liu, Y.; Chen, B., Exceptionally High Acetylene Uptake in a Microporous Metal-Organic Framework with Open Metal Sites. *J. Am. Chem. Soc.* **2009**, *131*, 12415-12419.
- (50) Zhang, M.; Li, B.; Li, Y.; Wang, Q.; Zhang, W.; Chen, B.; Li, S.; Pan, Y.; You, X.; Bai, J., Finely tuning MOFs towards high performance in C₂H₂ storage: synthesis and properties of a new MOF-505 analogue with an inserted amide functional group. *Chem. Commun.* **2016**, *52*, 7241-7244.
- (51) Cui, X.; Chen, K.; Xing, H.; Yang, Q.; Krishna, R.; Bao, Z.; Wu, H.; Zhou, W.; Dong, X.; Han, Y.; Li, B.; Ren, Q.; Zaworotko, M. J.; Chen, B., Pore chemistry and size control in hybrid porous materials for acetylene capture from ethylene. *Science* **2016**, *353*, 141-4.
- (52) Wen, H.-M.; Wang, H.; Li, B.; Cui, Y.; Wang, H.; Qian, G.; Chen, B., A Microporous Metal-Organic Framework with Lewis Basic Nitrogen Sites for High C₂H₂ Storage and Significantly Enhanced C₂H₂/CO₂ Separation at Ambient Conditions. *Inorg. Chem.* **2016**, *55*, 7214-7218.
- (53) Jiao, J.; Dou, L.; Liu, H.; Chen, F.; Bai, D.; Feng, Y.; Xiong, S.; Chen, D. L.; He, Y., An aminopyrimidine-functionalized cage-based metal-organic framework exhibiting highly selective adsorption of C₂H₂ and CO₂ over CH₄. *Dalton Trans.* **2016**, *45*, 13373-13382.
- (54) Moreau, F.; da Silva, I.; Al Smail, N. H.; Easun, T. L.; Savage, M.; Godfrey, H. G.; Parker, S. F.; Manuel, P.; Yang, S.;

- Schroder, M., Unravelling exceptional acetylene and carbon dioxide adsorption within a tetra-amide functionalized metal-organic framework. *Nat. Commun.* **2017**, *8*, 14085.
- (55) Yang, S.; Ramirez-Cuesta, A. J.; Newby, R.; Garcia-Sakai, V.; Manuel, P.; Callear, S. K.; Campbell, S. I.; Tang, C. C.; Schröder, M., Supramolecular binding and separation of hydrocarbons within a functionalized porous metal–organic framework. *Nat. Chem.* **2015**, *7*, 121-129.
- (56) Song, C.; Jiao, J.; Lin, Q.; Liu, H.; He, Y., C₂H₂ adsorption in three isostructural metal-organic frameworks: boosting C₂H₂ uptake by rational arrangement of nitrogen sites. *Dalton Trans.* **2016**, *45*, 4563-4569.
- (57) Ye, Y.; Ma, Z.; Chen, L.; Lin, H.; Lin, Q.; Liu, L.; Li, Z.; Chen, S.; Zhang, Z.; Xiang, S., Microporous metal–organic frameworks with open metal sites and π -Lewis acidic pore surfaces for recovering ethylene from polyethylene off-gas. *J. Mater. Chem. A* **2018**, *6*, 20822-20828.
- (58) Liu, K.; Ma, D.; Li, B.; Li, Y.; Yao, K.; Zhang, Z.; Han, Y.; Shi, Z., High storage capacity and separation selectivity for C₂ hydrocarbons over methane in the metal–organic framework Cu–TDPAT. *J. Mater. Chem. A* **2014**, *2*, 15823-15828.
- (59) Chen, F.; Bai, D.; Wang, X.; He, Y., A comparative study of the effect of functional groups on C₂H₂ adsorption in NbO-type metal–organic frameworks. *Inorg. Chem. Front.* **2017**, *4*, 960-967.
- (60) Xue, Y.-Y.; Bai, X.-Y.; Zhang, J.; Wang, Y.; Li, S.-N.; Jiang, Y.-C.; Hu, M.-C.; Zhai, Q.-G., Precise Pore Space Partitions Combined with High-Density Hydrogen-Bonding Acceptors within Metal–Organic Frameworks for Highly Efficient Acetylene Storage and Separation. *Angew. Chem. Int. Ed.* **2021**, *60*, 10122-10128.
- (61) Rao, X.; Cai, J.; Yu, J.; He, Y.; Wu, C.; Zhou, W.; Yildirim, T.; Chen, B.; Qian, G., A microporous metal–organic framework with both open metal and Lewis basic pyridyl sites for high C₂H₂ and CH₄ storage at room temperature. *Chem. Commun.* **2013**, *49*, 6719-6721.
- (62) He, Y. B.; Krishna, R.; Chen, B. L., Metal-organic frameworks with potential for energy-efficient adsorptive separation of light hydrocarbons. *Energy Environ. Sci.* **2012**, *5*, 9107-9120.
- (63) Wang, F.; Kusaka, S.; Hijikata, Y.; Hosono, N.; Kitagawa, S., Development of a Porous Coordination Polymer with a High Gas Capacity Using a Thiophene-Based Bent Tetracarboxylate Ligand. *ACS Appl. Mater. Interfaces* **2017**, *9*, 33455-33460.
- (64) Hu, Y.; Xiang, S.; Zhang, W.; Zhang, Z.; Wang, L.; Bai, J.; Chen, B., A new MOF-505 analog exhibiting high acetylene storage. *Chem. Commun.* **2009**, 7551-7553.